Design of a Wideband Wide-angle Scanning Dielectric Resonator Antenna Array with Additive Manufacturing Capabilities for Satcom

Keshav Anand Nair

TUDelft

Design of a Wideband Wide-angle Scanning Dielectric Resonator Antenna Array with Additive Manufacturing Capabilities for Satcom

by

Keshav Anand Nair

To obtain the degree of Master of Science in Electrical Engineering
at the Delft University of Technology,
to be defended publicly on Monday August 21, 2023 at 13:30.

An electronic version of this thesis is available at `http://repository.tudelft.nl/`

Cover page image: `https://www.istockphoto.com/`

ŤUDelft

MS³ Microwave Sensing Signals & Systems

DLR Deutsches Zentrum für Luft- und Raumfahrt German Aerospace Center

Acknowledgements

Abstract

The mm-wave operational band (24-30 GHz) is becoming increasingly important for various practical applications. However, at such high frequencies, the issue of propagation losses arises, emphasizing the necessity for these systems to achieve high radiation efficiency. Dielectric Resonator Antennas (DRA) are promising candidates to replace traditional radiating elements like patches since they do not suffer from conductor losses and have a radiation efficiency of over 90% when suitably excited. Additive manufacturing has emerged as a promising technique for producing DRAs due to its numerous benefits, such as the ability to fabricate complex shapes and structures, rapid prototyping, and reduced waste. Additionally, 3D printing can enable the incorporation of varying permittivities within the DRA, further enhancing its performance. The influence of such permittivity profiles in DRAs, particularly in finite phased array setups, is yet to be thoroughly investigated. It is important to understand the impact of this technique on the mutual coupling, cross-polarization, and scanning performance of the array. In this work, we discuss the theory behind the radiation characteristics, the modelling of the DRA designs and the analyses of these designs based on performance criteria such as bandwidth, coupling, gain, cross-polarization and axial ratio bandwidth. This thesis demonstrates for the first time, to the best of author's knowledge, that the incorporation of permittivity profiles in mm-wave DRAs can improve the bandwidth by 7%, reduce the cross-polarization (at $\theta = 0^\circ$) by around 3 dB and improve the axial ratio bandwidth by around 10% compared to single-permittivity DRAs. Furthermore, it is also shown that in an array environment, the active S-parameters of the elements are better matched across a wider frequency band, upon scanning from 0° to 45°, when a permittivity profile is used.

Contents

List of Figures

List of Tables

Nomenclature

Abbreviations

Abbreviation	Definition
AM	Additive Manufacturing
AR	Axial Ratio
CDRA	Cylindrical Dielectric Resonator Antenna
CP	Circular Polarization
DRA	Dielectric Resonator Antenna
DR	Dielectric Resonator
FDM	Fused Deposition Modelling
HEM	Hybrid Electric and Magnetic
LHCP	Left Hand Circular Polarization
LP	Linear Polarization
RHCP	Right Hand Circular Polarization
SATCOM	Satellite Communication
SLA	StereoLithography
TE	Transverse Electric
TM	Transverse Magnetic

<div align="right">

1

</div>

<div align="right">

Introduction

</div>

1.1. Motivation

Over the past few decades, considerable research has gone into the field of Dielectric Resonator Antennas (DRAs). The study on DRAs as an alternative to the microstrip patch was kick-started by Long et al. [1], and it has been studied extensively ever since. A DRA is primarily a 3D antenna that makes use of the radiating properties of a dielectric resonator (Figure 1.1). The absence of conductor and surface wave losses have made it an attractive option for a myriad of applications at high frequencies (mm-wave band). DRAs make use of radiating resonators to transform guided waves into unguided waves. Moreover, they have high radiation efficiency and improved bandwidths, compared to conventional patch antennas. The high radiation efficiency was demonstrated by [2], where an aperture-coupled cylindrical DRA attained efficiency values of 93% as opposed to a lower efficiency of 82% obtained from a patch antenna with the same type of feeding. The improved bandwidth can be attributed to the fact that the DRA radiates through the whole DRA surface except the grounded part. The gain and polarization characteristics can also be easily tailored based on the requirements by using various design techniques, such as parasitic patches, multiple feeds, or multi-layered DRA geometries. High dielectric permittivity can facilitate miniaturization of the antenna structure. The mechanical and thermal stability of DRAs enable easy integration with electrical circuits. All these benefits make DRAs strong contenders for mm-wave applications and this forms the motivation for this thesis. However, DRAs are bulkier than patch antennas, which means they take up more space and are more complex to fabricate using conventional manufacturing techniques.

DRAs are typically manufactured using dielectric materials of dielectric permittivity ϵ_r as low as 3 and up to 100. High values of ϵ_r lead to a decrease in bandwidth while enabling a reduction in the size of the antenna [5]. High dielectric-constant materials can considerably reduce the size of the DRA, since the DRA size is proportional to $\lambda_0/\sqrt{\epsilon_r}$, λ_0 being the free-space

Figure 1.1: Dielectric Resonator Antennas [3, 4]

wavelength. This means the DRA can maintain high radiation efficiency in the millimeter-wave band for applications including automotive radars, satellite communications and 5G base stations. Although most DRAs studied have conventional geometries like cylindrical or rectangular, more unconventional shapes like pyramidal, hemispherical or super-shapes have also been explored [5]. In addition, the use of multiple resonating bodies has also received much attention [6]. Herein anisotropic or inhomogeneous permittivity can be introduced into the design as a degree of freedom. However, manufacturing such a design via conventional PCB manufacturing techniques becomes unreliable as the effect of glues and tolerances need to be incorporated into the design process.

Similar to a patch, multiple feeding techniques can be employed with a DRA, depending on the requirements. Popular feeding techniques include probe-fed, microstrip transmission line fed and slot-fed. Substrate integrated waveguide (SIW) cavity with a slot is also an attractive method, however, the manufacturing and realization of such a design becomes more complex. The study and use of additive manufacturing (AM) in 3D printing antennas, particularly DRAs, have gained a lot of traction in recent years (Figure 1.2). This allows greater customization and faster prototyping. It also enables the manufacturing of unconventional geometries with greater precision. Moreover, spatial variation of permittivities along the vertical or radial direction can be achieved relatively easily by employing additive manufacturing techniques.

Figure 1.2: 3D printed multi-ring DRA with spatial variation in permittivity [7]

1.2. Problem Formulation

Despite the vast amount of literature on DRA elements and additive manufacturing, the full potential of 3D printing in the design of dielectric resonator antennas with permittivity profiles is yet to be explored. Additionally, the limited literature on additively manufactured DRAs focuses primarily on single elements. At the same time, they have great potential in their use for small-sized and large-sized linear and planar arrays, which forms the motivation for this thesis project. Moreover, a comparative study of different permittivity profiles is lacking. The advantages of these profiles in an array environment are also yet to be studied. Many modern wireless applications require wideband and wide-scanning phased arrays. This requires revisiting the DRA unit cell design and optimization within an array environment, including a study on the coupling effects among the DRA elements and their performance.

1.3. Objectives

The available literature discusses techniques for improving the various performance parameters of DRAs. Gain enhancement can be obtained by integrating additional structures or exciting higher-order modes in the dielectric resonator (DR). Bandwidth can be expanded by combining different DRs, choosing appropriate geometries or feeding slots. Circular polarization can be achieved using dual feeds, single feed with parasitic patch or slot fed with the DR rotated with respect to the slot. However, these techniques are based on conventional manufacturing techniques, and the full utilization of additive manufacturing techniques to fabricate DRAs is yet to be investigated extensively. Furthermore, the impact of additively manufactured DRA elements in an array environment has not been looked into yet. **This master thesis aims to:**

- **Provide a fair comparative analysis of permittivity profiles**
- **Compare the performance of DRAs with permittivity profiles against a benchmark model with homogeneous permittivity**
- **Evaluate these results in an array environment.**

1.4. Scope

A multitude of geometries and feeding techniques were explored in literature for various applications (Section 2.2). The primary design selections are motivated in Section 2.4. In this work, to keep the focus on permittivity profiles, these unconventional shapes are not considered and a cylindrical geometry is used. This is motivated by the fact that multiple modes can be excited with better flexibility as opposed to other geometries. Moreover, fabrication is easier for such geometries. As the primary application of interest here is SATCOM, a circularly polarized design is investigated, together with dual linear polarization for completeness. For simulation purposes, a dual probe feeding was employed to study the coupling effects. The probes are placed closer to the periphery of the DR to excite the required mode. It is challenging to incorporate a probe feeding at higher frequencies, as drilling holes and positioning the DRA lead to fabrication complexities. As the primary focus here is to investigate and analyze the impacts of employing a permittivity profile in a DRA, much importance is not given to the

practical constraints of the feeding technique. Therefore, here we use two probes placed at $90°$ to each other and embedded in the DRA to generate circular polarization. To this extent, the effect of different permittivity profiles (linearly-nonlinearly increasing-decreasing) on the performance is investigated. A comparison of the performance between designs with a profile and a benchmark model without one is also carried out. Finally, an aperture-fed DRA is designed as proof-of-concept which can be easily fabricated.

1.5. Novelties

This thesis, for the first time proposes a novel use of additive manufacturing in the flexible realization of DRAs wherein various permittivity profiles are introduced in the DR elements (standalone and in an array). The impacts and benefits of the same in terms of bandwidth, coupling, co-polarization, cross-polarization and axial ratio bandwidth are studied at a single-element level. The array analysis includes the study of mutual coupling between the elements and the scan performance of the array. Moreover, a fair comparative analysis of mm-wave DRAs (with respect to the above-mentioned metrics) having such profiles with a benchmark DRA without profile is also presented (operational band: 25-35 GHz).

1.6. Thesis Structure

The rest of the thesis is organized as follows. Chapter 2 deals with a literature survey which helps dive deeper into the research on DRAs and identify the existing state-of-the-art designs. Chapter 3 revisits the theory where the various modes excited in a cylindrical DRA are studied and a suitable mode for operation is chosen. The various feeding techniques are also discussed. These chapters help identify a suitable geometry and feeding techniques for further simulations and analyses. Chapter 4 discusses the settings used for the simulations and the methodology followed for the realization of spatially varied permittivity on CST Microwave Studio. The illustrations of various designs are included for ease of visualization. Finally, in Chapter 5, the results from the simulations are put forward and the analyses are presented.

2

Literature Study on Dielectric Resonator Antennas

This chapter discusses the relevant approaches for controlling the circuital and radiation characteristics of a DRA. A combination of various geometries, feeding structures and methods for enhancing the **gain**, **impedance bandwidth** and **axial ratio bandwidth** (for circularly polarized DRAs) are discussed. To draw the focus to additive manufacturing, the literature study is organized into two sections, namely DRAs fabricated from conventional manufacturing and additive manufacturing techniques.

2.1. Overview

This literature study summarizes the relevant work available on DRAs. A deep survey of various geometries and feeding techniques is done and suitable design choices are made. Firstly conventional manufacturing techniques are discussed, starting with simple DR geometries like cylindrical and rectangular DRAs. Cylindrical DRAs are easier to fabricate but have less degrees of freedom when it comes to geometry. The attractiveness of rectangular DRAs is due to their better design flexibility and reduced cross-polarization levels compared to cylindrical DRAs [8]. A higher bandwidth and high gain are obtained by more complex DRA geometries called supershapes. The polarization of such geometries can be controlled easily by using single or dual feeds, or making use of cross slots [9, 10].

Stacking rectangular DRAs of varied permittivities and heights can facilitate the broadening of the impedance bandwidth due to the generation of multimode resonances in each layer. Such a design can be modified by introducing a metal patch on top of the DRA and using an SIW cavity with slot to attain a dual-band, dual circularly polarized configuration [11]. An effective way of obtaining an enhanced axial ratio bandwidth is by using a two-layer rectangular DRA, with the top layer rotated at an angle with respect to the layer below. Introducing a metal ring around a cylindrical DRA can enable a wide beam performance, while stacking dielectric slabs

on top can help shape the beam [12]. More details on all the designs are provided in the following section, with Table 2.1 summarizing the details.

Secondly the utilization of additive manufacturing in DRA production is discussed. These techniques help overcome the limitations of conventional fabrication. They allow for the elimination of bonding materials like glue and thereby help remove unwanted effects introduced by them. They also facilitate the easy fabrication of complex geometries like supershapes. 3D printed antennas are seen to achieve a high gain. Spatial variation of permittivity in the DR structure is also an effective technique to improve the bandwidth, which is made possible by recent advances in 3D printing techniques. In addition to obtaining a wider bandwidth, a high radiation efficiency is also achieved [7].

2.2. Conventional Manufacturing techniques

Conventional DRA shapes, primarily cylindrical and rectangular DRAs, have been studied extensively. **Cylindrical DRAs** are attractive owing to their ease of fabrication and the ability to excite different modes. G. Massie et al. present a simple circularly polarized DRA unit cell design operating around 1.5 GHz with a cylindrical DRA fed by four sequentially rotated slots as seen in Figure 2.1a [13]. This antenna had an impedance bandwidth of 44% with an axial ratio less than 0.1 dB. However, the gain was relatively low, with a value above 1.5 dBic across the band.

A more compact structure with simpler feeding was proposed by [14] where a cylindrical ring dielectric resonator is fed by a coaxial probe with the inner conductor adjacent to the DR for signal transition (Figure 2.1b). It was seen to have an excellent radiation efficiency of over 95%.

(a) Cylindrical DRA fed by four slots [13]

(b) Cylindrical DRA fed by coaxial cable [14]
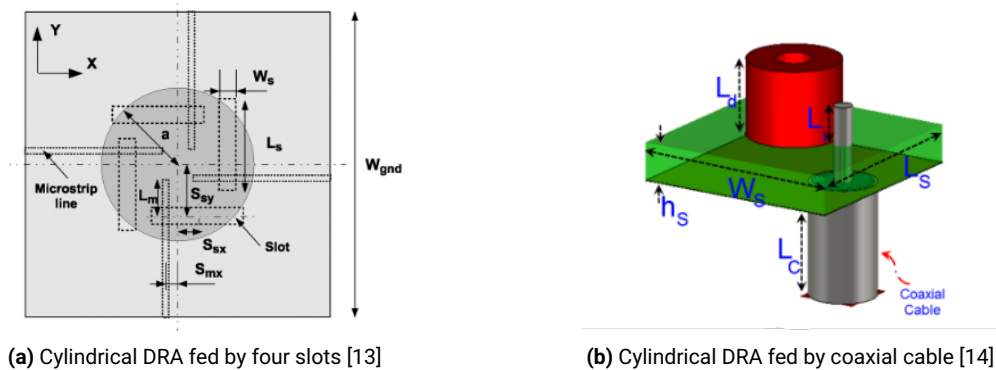
Figure 2.1: Cylindrical DRAs

The primary advantage of **rectangular DRAs** is that they can be characterised by three independent geometric dimensions of length, width and height, offering a better design flexibility [5]. In addition it is also characterized by low cross-polarization levels [15]. L.Y. Feng et al. examine the design of a rectangular DRA operating at around 28 GHz, with a wide bandwidth achieved by properly **combining two higher-order modes** (TE_{113} and TE_{115}) [16]. The DRA

is excited by means of a coaxial probe placed tangentially along one of the sides of the DRA (Figure 2.2a).

More unconventional shapes like a **pyramidal DRA** were explored by B. Liu et al. [17]. An inverted pyramid DRA fed by a rectangular slot aperture operating at 9-10 GHz is presented (Figure 2.2b). The DRA is rotated by 45° with respect to the slot to obtain left-handed CP.

(a) Rectangular DRA fed by coaxial probe [16]   **(b)** Pyramidal DRA fed by slot [17]
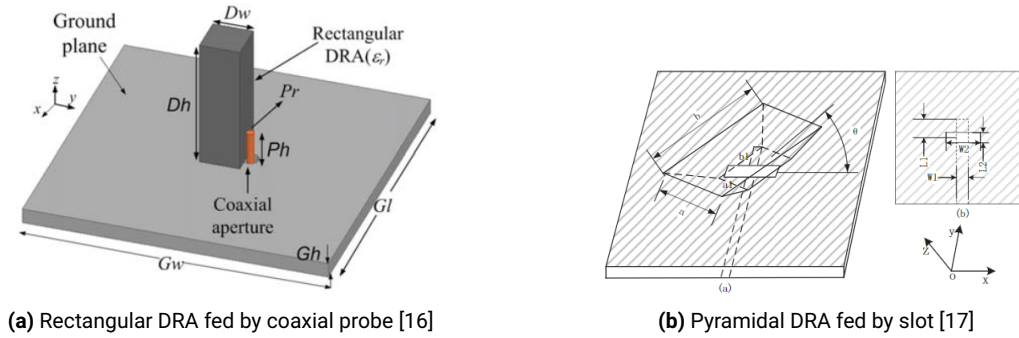
Figure 2.2: Rectangular and Pyramidal DRAs

More recently in the past decade, more complex DRA geometries namely **supershapes** have been explored [18]. The cross-section of such supershaped DRAs is described by means of the superformula proposed by J. Gielis in [19]. The superformula is essentially a generalization of the ellipse's polar equation. This opens the door to a wide variety of DRAs, due to the **increased degrees of freedom** for the DR geometry design. Such supershaped DRAs were shown to provide good flexibility in terms of radiation patterns while exhibiting wideband matching characteristics and broadside radiation [18].

A probe-fed plastic-based supershaped DRA of the structure shown in Figure 2.3a with sextet values of ($a = b = 1, m = 4, n_1 = n_2 = n_3 = 1/2$) was investigated by D. Caratelli et al. in [9]. It was designed to operate in the 10 GHz band yielding a high impedance bandwidth of 70% and an exceptional gain of 10 dBi. The polarization could be easily controlled by using a single feed (linear polarization) or dual feed (circular polarization). The circularly polarized design exhibited an axial ratio below the 3 dB level over a wide frequency range.

A **flower-shaped DRA** obtained from the superformula with the variable set of ($a = b = 1, m = 6, n_1 = 0.4, n_2 = 1, n_3 = 6$) is proposed in [10] (Figure 2.3b). It is fed by a cross slot and is circularly polarized, operating at a centre frequency of 30 GHz.

(a) Probe-fed plastic-based supershaped DRA [9]   **(b)** Flower-shaped DRA fed by cross slots [10]
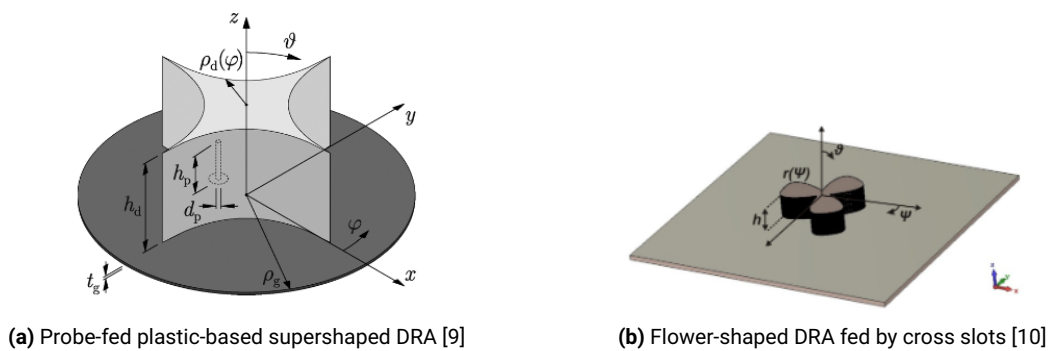
Figure 2.3: Supershaped DRAs

In the past few years, a simple but effective technique for expanding the bandwidth of a DRA has been inspected. Using a high permittivity dielectric enables reduction in size of the DR but reduces the operating bandwidth. Thus miniaturization and wide bandwidth of a single dielectric DRA are contradictory [6]. An effective way to mitigate this is to introduce **multiple dielectric layers with varied cross-sections and permittivities**. The different natural resonant frequencies for each layer lead to the generation of multimode resonances and thus the bandwidth will be improved.

In [6], F. Wang et al. propose a multilayer DRA with three layers of different heights and permittivities (Figure 2.4a). A coaxial probe is used to excite this DRA structure. In order to improve the impedance matching and optimize the return loss, a feeding patch made of copper is placed between the side of the DRA and the coaxial probe. It is circularly polarized operating at around 11 GHz and is seen to cover an ultrawide bandwidth 6-16 GHz (relative bandwidth of 90.9%). Moreover, this DRA has an attractive gain of 6.21 dB and a 3 dB beamwidth of $\pm 60°$ at 12 GHz.

An anisotropic rectangular DRA with 14 layers where each layer with thickness h_1 and permittivity ϵ_1 is separated by a layer of height h_2 and permittivity ϵ_2 is analyzed in [20]. The layers are combined using a very thin layer of instant glue. The anisotropic DRA is excited by a cross slot and a spiral microstrip line with phase delay (Figure 2.4b). Such a feed setup ensures that two orthogonal modes (TE_{111}^x and TE_{111}^y) are excited simultaneously, generating circular polarization. This configuration operates at 3.5 GHz, returning an impedance bandwidth of 31.43% and an axial ratio bandwidth of 20.29%. Moreover, a high average gain of 8 dBi is obtained over the operating band.

The use of two-layer rectangular DRA with the **top layer rotated at an angle** relative to the bottom one is found to be a simple yet effective technique to generate circular polarization with a single feed while maintaining a relatively high bandwidth [21]. A circularly polarized antenna using a rotated-stair dielectric resonator with a single aperture coupled feed is presented in [22]. A dual offset feed line is used to realize proper impedance matching (Figure 2.5a). The configuration has a low profile structure and was designed to operate at the 5.8 GHz band.

A similar configuration operating at around 28 GHz is discussed in [23], where a **cavity-backed SIW** (Substrate Integrated Waveguide) feeding is used to build the cavity in a single-layer substrate. (Figure 2.5b). The unit cell is fed using a coaxial cable probe, thus eliminating the need for an external feed network.

Various designs for more specific applications have also been discussed in literature. A novel **dual-band and dual-circularly polarized** stacked DRA was investigated by Z. Chen et al. in [11], for UAV satellite communications. Such an antenna configuration consists of a double-layer stacked rectangular DR, a SIW cavity with slot for feeding and a metal strip rotated at an angle with respect to the slot placed on top of the stacked DRA (Figure 2.6a). This strip is utilized for achieving circular polarization. The antenna operates at 20 and 30 GHz bands, in dual polarization with two orthogonal CPs in the respective bands. This paper presents a promising single-fed, compact DRA configuration achieving full duplex operation at two different bands. However, the bandwidths in both bands are quite low at 6% and 12%, respectively.
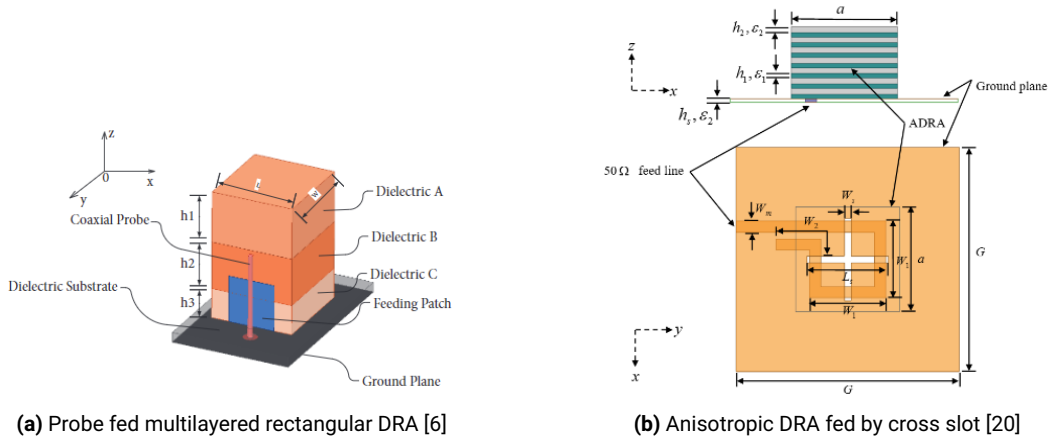
(a) Probe fed multilayered rectangular DRA [6]

(b) Anisotropic DRA fed by cross slot [20]

Figure 2.4: Multilayered rectangular DRAs
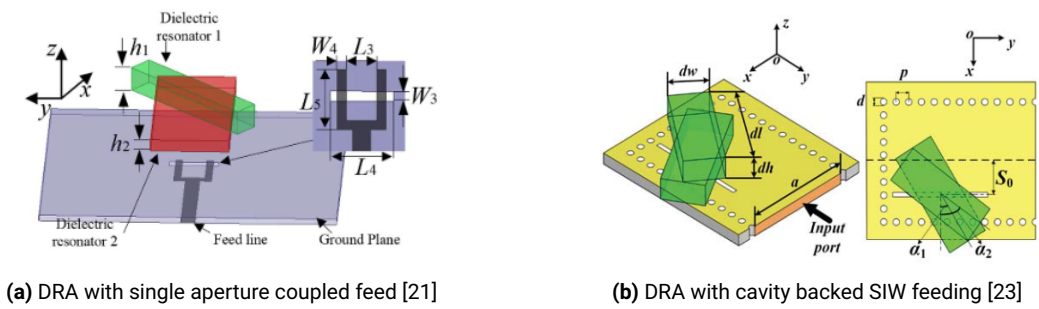
(a) DRA with single aperture coupled feed [21]

(b) DRA with cavity backed SIW feeding [23]

Figure 2.5: Rotated stair rectangular DRAs

An innovative technique to **alleviate the severe gain drop during beam steering** is put forward by K.W. Leung et al. in [12]. The proposed design consists of a cylindrical DRA (permittivity ϵ_1) mounted on top of a PCB. The DRA is excited by means of a rectangular slot and a microstrip line. A **metal ring** surrounding the DRA is placed on the PCB to introduce a central dip in the radiation pattern and thus obtain a **wide beam performance**. To further adjust the shape of the centre dip, two additional dielectric slabs (permittivities ϵ_2 and ϵ_1, respectively) are placed on top of the DRA. The unit cell geometry can be viewed in Figure 2.6b. Very wide 3 dB beamwidths of 172° and 149° are observed in the E- and H- planes, respectively. The peak realized gain varies between 3.2 and 4.6 dBi.
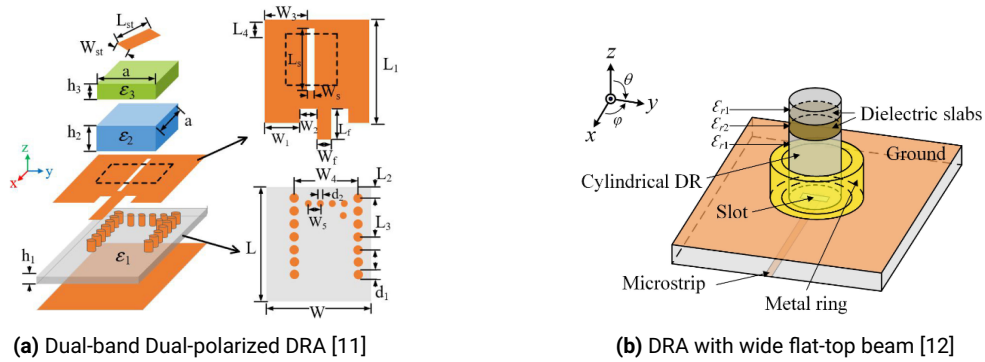
(a) Dual-band Dual-polarized DRA [11]

(b) DRA with wide flat-top beam [12]

Figure 2.6: Novel DRAs for specific applications

Literature	Geometry	Feeding technique	Frequency of operation (GHz)	Gain (dBi)	Bandwidth (%)	Polarization	Axial Ratio Bandwidth (%)
[13]	Cylindrical	Sequentially rotated 4 slots	1.5	1.5	44	Circular	-
[14]	Cylindrical ring	Coaxial probe	27	4	>50	Linear	-
[24]	Cylindrical	Slot feed	30	9	6.6	Linear	-
[16]	Rectangular	Coaxial probe	28	8.66	26.4	Linear	-
[17]	Inverted pyramid	Slot feed	9-10	6.8	45.8	Circular	8.9
[9]	Supershape	Dual probe fed	10	10	70	Circular	-
[10]	Flower shaped	Cross slot	33.8	9.5	33.8	Circular	5
[6]	Rectangular stacked	Coaxial probe and feeding patch	11	6.2	90.9 (-below 8 dB)	Linear	-
[20]	Rectangular anisotropic	Cross slot with spiral feed line	3.5	8	31.4	Circular	20.2
[21]	Stacked rectangular	Slot with dual offset feed line	5.8	4.5	31	Circular	18
[23]	Stacked rectangular (4x4 array)	Cavity backed SIW feed	28	16	1.5	Circular	-
[11]	Double layer rectangular	SIW cavity with slot	20, 30 (dual-band)	6.6-8.2	6.4, 12.8	Dual Circular	5.2, 4.1
[12]	Stacked cylindrical	Slot feed	10.65	3.2-4.6	13.5	Linear	-

Table 2.1: Conventionally manufactured DRAs

2.3. Additive Manufacturing Techniques

3D printing or additive manufacturing is a concept that has been widely discussed over the past decade. This technology has received great attention in the development of RF elements, including antennas [25]. DRAs with their inherent dielectric nature help overcome the challenge of prototyping conductive parts in manufacturing fully 3D-printed antennas. The most popular and cost-effective 3D printing techniques include **Stereolithography** (SLA) and **Fused Deposition Modeling** (FDM) [26]. SLA uses a liquid resin, namely photopolymers that solidify when exposed to an ultraviolet laser beam. In case of FDM, the material is melted through an extrusion nozzle and deposited layer by layer. SLA can achieve higher accuracy with reduced surface roughness. However, the material costs are high. On the other hand, FDM is simple, cost-effective and does not require post-processing. Additive manufacturing allows for the rapid development of antennas at a low cost. Moreover, it also eliminates the need for bonding materials like glue during the fabrication of multilayered dielectric antennas.

The application of additive manufacturing in fabrication of DRAs has been discussed briefly in literature. A dual-polarized 3D-printed DRA is presented in [27]. The square base area enables the rectangular DRA to support two orthogonal linearly polarized modes. A cross slot with two feed lines excite the two orthogonal modes. To avoid overlap of the lines, the ends follow a fork structure (Figure 2.7a). An array of 2x2 elements is fabricated and its performance is analyzed at 28 GHz. It is seen to achieve a gain of 8.49 dBi and a fractional bandwidth of 11%.

An unconventionally shaped wideband DRA was designed by R. Colella et al. in [28]. The geometry consists of two rectangular DR elements of increasing size stacked one on top of the other. A **rounded fillet** is applied to the edges at the centre of the DR to enable gain and bandwidth improvement by smoothing the transition of the EM field between the elements (Figure 2.7b). Furthermore, a metal patch is placed on top to achieve linear polarization while expanding the bandwidth. The fabrication is done by employing the FDM technique and a microstrip feed slot is used to excite the DR. The antenna was seen to operate at 2.45 and 3.6 GHz bands with the respective gains being 5.45 and 6.38 dBi. The fractional bandwidth was slightly less than 46%. The E- and H- plane 3 dB beamwidths were observed to be around 96° and 74° respectively.

Spatial variation of permittivity, as opposed to tailored geometries, was introduced to improve the bandwidth [29]. Advances in additive manufacturing enable the fabrication of simple geometries with complex distribution of material properties. Tailored material properties are attained by custom fabricating filaments loaded with powders thus forming composite structures. The design put forward in [29] includes a **flipped step stair-shaped** cuboidal DRA structure, as seen in Figure 2.8a. The DRA is excited by a microstrip feed line and a narrow slot aperture. The antenna operates in the X band (around 10 GHz) achieving a wide impedance bandwidth of 60% and a gain of over 6.5 dB across the operating band.

K.W. Leung et al. investigated a 3D-printed **multi-ring DRA** for the first time in [7]. The geometry consists of four concentric dielectric rings with different air-filling ratios to obtain different

(a) 3D printed rectangular DRA [27]   **(b)** Unconventional shaped DRA [28]
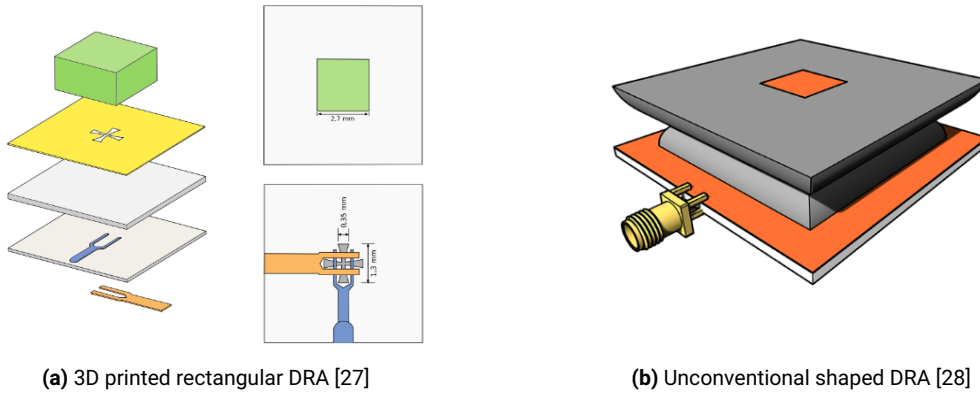
Figure 2.7: 3D printed DRAs

dielectric constants (Figure 2.8b). The DRA is mounted on a circular ground plane and a coax-ial cable penetrating into the DRA is used to excite the three TM modes ($TM_{01\delta}$, $TM_{02\delta}$ and $TM_{03\delta}$). The antenna is designed to operate in the C band (around 6.15 GHz), providing a wide bandwidth of 60.2% and an average radiation efficiency of 89%. Nevertheless the gain is quite low, varying between 0.65 and 2.45 dBi across the band.

(a) Flipped step stair cuboidal DRA [29]   **(b)** Multi-ring DRA [7]
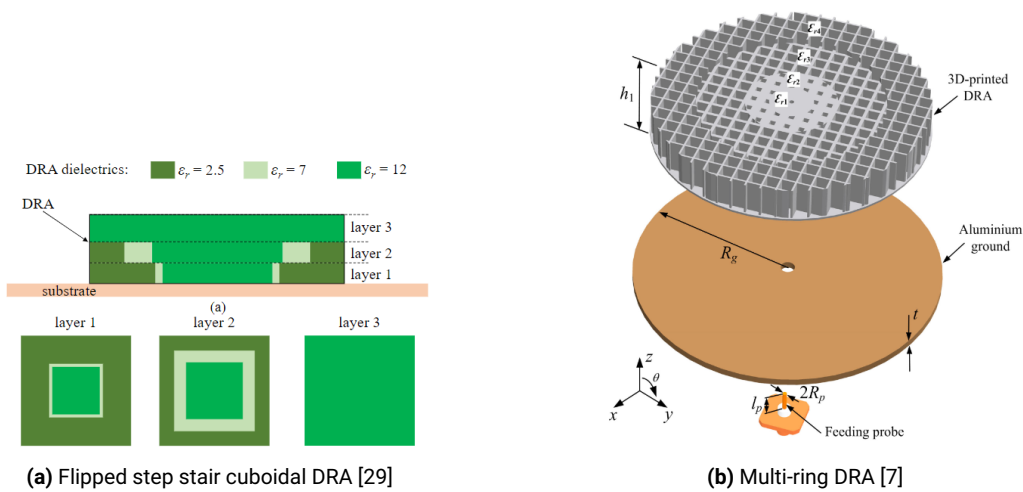
Figure 2.8: DRAs with spatial permittivity variation

A similar geometry with a slight variation in the geometry is proposed in [30], where two **air ring layers** are inserted between the concentric dielectric rings (2.9). This design, operating at 5.3 GHz had a slightly higher impedance bandwidth of 65.7% and a higher gain, varying between 1.8 - 4.1 dBi across the band.

2.4. Conclusion

The literature review discussed various techniques employed in the design of DRAs. As men-tioned in Section 1.4, the choice of geometry is narrowed down to cylindrical. This is motivated by the fact that multiple modes can be excited with better flexibility compared to other geome-
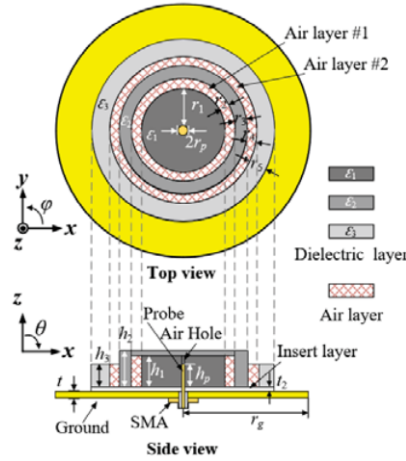
Figure 2.9: Multi ring DRA with air gaps [30]

tries [5]. Moreover, fabrication is easier for such geometries. Furthermore, to keep the focus on permittivity profiles, we do not dive deeper into the unconventional geometries. The feeding techniques considered are probe feed and aperture coupling as they are the simplest and most effective methods. For simulation purposes, a probe-fed configuration is used as the design is relatively simpler with lesser degrees of freedom. Moreover, using a dual-probe configuration to attain circular polarization enables analysis of the coupling between the ports upon excitation. Ultimately, an aperture-fed DRA is designed as a viable proof-of-concept demonstration, which is relatively easy to manufacture.

Various techniques to improve the bandwidth and gain of DRAs are presented in literature. However, **minimal literature exists on the use of additive manufacturing in DRA production**. Moreover, they only discuss the realization of multi-layered or multi-ringed DRAs with a step change in permittivity. The **adoption of swept permittivity in DRAs has yet to be explored**. Advances in additive manufacturing have enabled spatial variation of permittivity in radial and vertical directions in a progressive and controlled manner. A study on the benefits of tailored permittivity in mm-wave DRAs as opposed to conventional DRAs with homogeneous permittivity is lacking. Additionally, **the existing body of literature lacks comprehensive research on the performance of such elements in an array setting**. This thesis presents a novel design flow wherein permittivity profiles are incorporated in an additively manufactured DRA. Unlike certain designs in literature, the design presented here does not make use of parasitic metal patches or any additional structures to improve impedance matching. To close these gaps in literature, **this thesis presents the first comparative analysis of varied permittivity profiles and how they fare against a benchmark DRA without a profile**. The array performance, primarily the performance of the edge elements and the coupling between the ports will also be investigated. Finally as a proof of concept, models for fabrication are also designed.

3

Theroretical Background

The development of dielectric resonators, which essentially serve as energy storage devices due to their high dielectric constant and high quality factor Q, gave rise to the dielectric resonator antenna [31]. Electromagnetic energy introduced into the dielectric block creates electromagnetic waves that bounce back and forth between the walls of the cavity thus leading to the formation of standing waves. The dielectric constant of the material must be large (typically 50 or greater) for the dielectric resonator to function as a resonant cavity. Here, the dielectric-air interface behaves as an open circuit, causing internal reflections that confine energy in the dielectric material, resulting in a resonant structure. A plane-wave approximation can be used to show this effect by looking at the reflection coefficient Γ at a dielectric-air interface [32]:

$$\Gamma = \frac{\eta_0 - \eta}{\eta_0 + \eta} = \frac{\sqrt{\epsilon_r} - 1}{\sqrt{\epsilon_r} + 1} \rightarrow 1 \quad \text{as } \epsilon_r \rightarrow \infty \tag{3.1}$$

To allow part of the energy from inside the cavity to escape through the cavity walls and cause radiation, the dielectric constants of the blocks of dielectric material must be in the range of 5-30.

Cylindrical DRAs (CDRA) are a popular choice of geometry for a variety of applications. This is due to its ease of fabrication and the ability to excite different modes [5], enabling varied radiation patterns depending on the application.

A simple structure of a probe-fed CDRA placed on a ground plane is shown in Figure 3.1. The resonant frequency and Q factor of the CDRA can be controlled easily by modifying the dielectric constant ϵ_r and the radius/height (a/h) ratio. Moreover, by adjusting the position and type of excitation, different modes can be excited leading to omnidirectional or broadside radiation patterns.
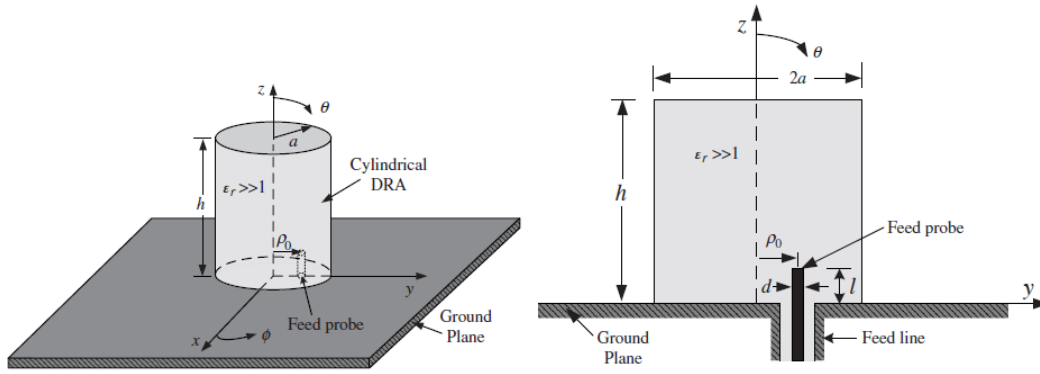
Figure 3.1: Probe-fed Cylindrical DRA [1]

3.1. Modes Excited in a Cylindrical Dielectric Resonator Antenna

Modes are the electromagnetic patterns inside the DRA existing due to the shape and boundary conditions. The various modes in a DRA can be excited by using appropriate feeding techniques. Modes excited in a DRA are crucial as they decide the radiation pattern and the efficiency of radiation. Such modal analysis is done using the cavity resonant model where the outer surfaces of the cavity are approximated as a perfect magnetic conductor. The primary natural modes in a CDRA include $TE_{mn\delta}$, $TM_{mn\delta}$ and $HEM_{mn\delta}$, where m, n and δ denote the field variations along the azimuthal, radial and axial directions respectively. The δ here is a non integer meaning the field variations along z are not full periods. Such field alterations within the CDRA are symmetric azimuthally (ϕ-independent) for the $TE_{mn\delta}$ and $TM_{mn\delta}$ modes, but not for the $HEM_{mn\delta}$ mode [33, 34].

At high frequencies, pure TE and TM modes do not exist distinctively. $HEM_{mn\delta}$ are hybrid modes with non-vanishing electric and magnetic components along the direction of propagation. The various modes can be excited by means of different feed techniques and from an application point of view, the most common radiating modes include $TE_{01\delta}$, $TM_{01\delta}$ and $HEM_{11\delta}$. These modes have low radiation Q-factor as they radiate with higher efficiency. The radiated field patterns vary significantly depending on the excited modes. Field distributions inside the DRA for these modes are shown in Figure 3.5 below, where the solid lines represent the E fields and the dotted ones represent the H fields.

The simplified expressions for the resonant frequency of these modes are given below:

$TE_{01\delta}$ -

$$f_r = \frac{v_o}{2\pi a}\left(\frac{2.327}{\sqrt{\varepsilon_r + 1}}\right)\left[1 + 0.2123\left(\frac{a}{h}\right) - 0.00898\left(\frac{a}{h}\right)^2\right] \tag{3.2}$$

$TM_{01\delta}$ -

$$f_r = \frac{v_o}{2\pi a}\left(\frac{1}{\sqrt{\varepsilon_r + 2}}\right)\sqrt{\left[(03.83)^2 + \left(\frac{\pi}{2}\right)^2\left(\frac{a}{h}\right)^2\right]} \tag{3.3}$$
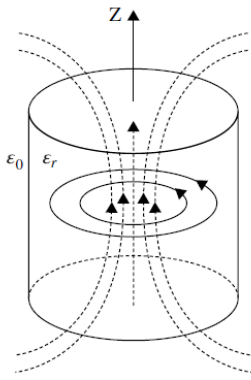
Figure 3.2: $TE_{01\delta}$
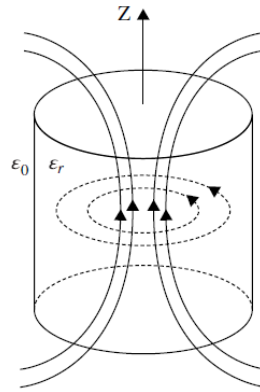
Figure 3.3: $TM_{01\delta}$
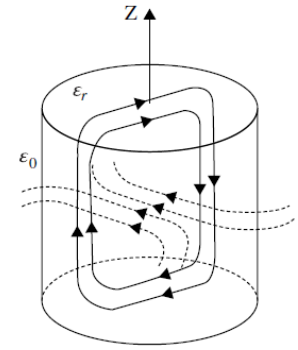
Figure 3.4: $HEM_{11\delta}$

Figure 3.5: Common modes in a CDRA [31]

$HEM_{11\delta}$ -

$$f_r = \frac{v_o}{2\pi a} \left(\frac{6.324}{\sqrt{\varepsilon_r + 2}} \right) \left(0.27 + 0.18z + 0.005z^2 \right) \tag{3.4}$$

For an isolated CDRA, the resonant frequencies of these modes can be arranged as $TE_{01\delta}$ < $TM_{01\delta}$ < $HEM_{11\delta}$

The corresponding radiation patterns of the modes are viewed in the figures below in Figure 3.6. $TE_{01\delta}$ radiation is equivalent to that of a short horizontal magnetic monopole, whereas that of $HEM_{11\delta}$ was typical of that of a magnetic dipole. Both these modes radiate in the broadside direction. Now the $TM_{01\delta}$ radiates in endfire and the pattern is similar to that of an infinitesimal electric dipole oriented vertically.
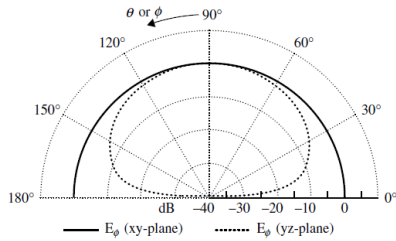
(a) $TE_{01\delta}$ Pattern
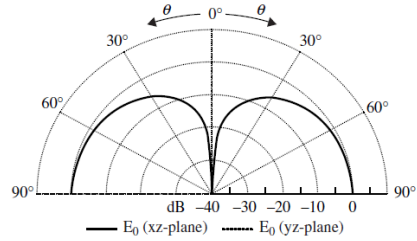
(b) $TM_{01\delta}$ Pattern
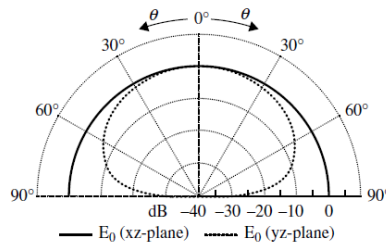
(c) $HEM_{11\delta}$ Pattern

Figure 3.6: Radiation patterns of the different modes [31]

3.2. Feeding Techniques

3.2.1. Aperture Coupling

Here, the feeding network is placed below the substrate thus preventing unwanted radiation that distorts the radiation pattern and improving the overall polarization purity of the antenna. This means lower cross-polarization levels and higher gain. For a DRA centered over a slot, the aperture is equivalent to a magnetic current flowing parallel to its length, thus exciting magnetic fields in the DRA leading to broadside radiation. The slot dimensions are chosen so that its resonance does not affect that of the DRA and enough to couple energy to the DRA structure. Positioning the slot towards the DRA boundary generates endfire radiation.
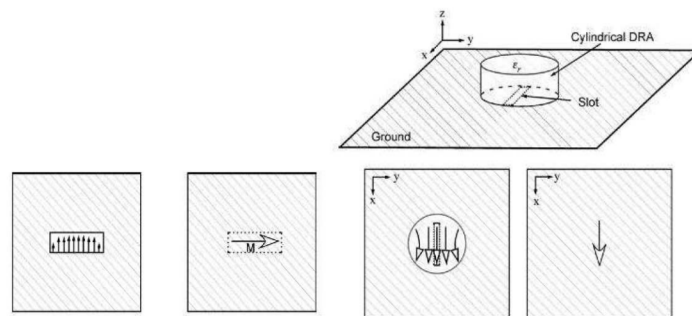
Figure 3.7: Fields in a slot-fed CDRA [35]

3.2.2. Coaxial Feeding

The probe can be considered equivalent to an electric current positioned vertically, enabling strong coupling to the DRA. The primary benefit of having a probe penetrating the DRA is that it ensures high coupling to the dielectric resonator leading to improved radiation efficiencies. The modes excited depend on the DRA shape and the probe position. Positioning the probe towards the periphery of the DRA whether embedded inside or placed outside the boundary generates a broadside pattern by exciting the $HEM_{11\delta}$ mode. Now if the probe is moved gradually towards the centre of the DRA, this mode diminishes and the $TM_{01\delta}$ dominates, exhibiting an endfire radiation pattern. However, proper selection of feed position by drilling holes and insertion of the metal probe in DRAs results in fabrication complexity.
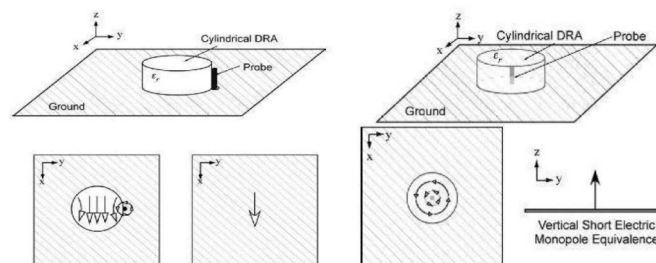
Figure 3.8: Fields in a probe fed CDRA [35]

3.3. Circular Polarization

Polarization is described as the motion of the electric field vector at a fixed position as a function of time. Typically, the polarization varies with different parts of the pattern as the polarization of the transmitted wave varies with the radiation from the centre of the antenna. The polarization pattern is the spatial distribution over an antenna's radiation sphere. All points on the radiation sphere can be resolved into a pair of orthogonal polarizations, namely co-polarization and cross-polarization. Co-polarization denotes the polarization that the antenna is intended to radiate whereas the latter is the orthogonal component. It is desired to have a cross-pol that is significantly lower than the co-pol for efficient radiation.

Although LP (Linearly Polarized) DRAs have been explored broadly in literature, they face a few drawbacks. Such antennas can only detect signals from a single direction and face polarization mismatch losses when signals arrive from different angles [36]. This means that the transmitting and receiving antennas have to be appropriately aligned.

The disadvantages of LP antennas are overcome by using a circularly polarized (CP) antenna as it can receive a component of the signal regardless of receiver orientation. Thus CP antennas are capable of transmitting and receiving signals in all planes without loss in strength of the signal. This helps mitigate multipath effects to a certain extent and also improve the gain and overall performance of the system. Moreover, the immunity to multipath-fading, better weather penetration, and imporved mobility than LP antennas make CP antennas an attractive option for various applications.

3.3.1. Feeding techniques for CP

Dual feeding is a relatively simple and effective technique to achieve circular polarization while maintaining a low axial ratio and a wide AR bandwidth. This is achieved by using quadrature signals fed into the DRA thereby exciting two orthogonal degenrate modes. The ports can be a dual probe feed configuration, two slots or confromal microstrip lines. To maintain a good axial ratio bandwidth, a high isolation between the feed points of the DRA is required.
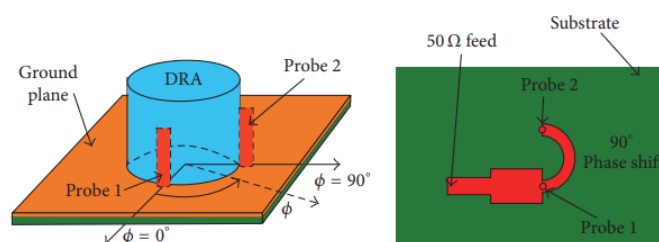
Figure 3.9: Dual probe feed configuration [5]

Single fed configurations have also been explored in literature, however they suffer from a narrow 3-dB axial ratio bandwidth. To this end cross slots can be used to excite two equal and orthogonal modes generating circular polarization. A design where an offset cross slot was used to excite a cylindrical DRA but with a narrow AR bandwidth of 4.8% was explored in [37].

The slot is rotated at $45°$ with respect to the DRA. Another technique for achieving CP with a single feed is by making use of a parasitic metal patch attached to the DRA surface. This leads to an assymmetry in the DRA geometry resulting in the excitation of two orthogonal modes with required phase shift [38]. This technique however returns a very narrow AR bandwidth, as demonstrated by [39] where an AR bandwidth of 2.2% was obtained. The feeding network in a single fed configuration is much simpler as for dual fed DRA, the need for an external quadrature coupler increases the system complexity.
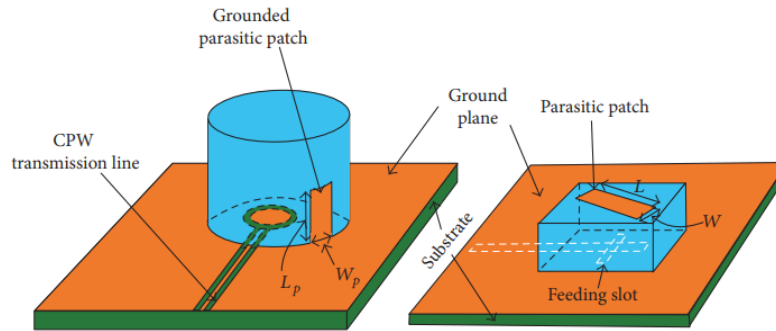
Figure 3.10: Single feed configuration with parasitic patch [5]

3.3.2. Sequential Rotation

An effective approach to improve the polarization purity of circularly polarized antenna elements is by using a sub-array where the single elements are sequentially rotated by $90°$ with respect to each other and also fed with a corresponding $90°$ phase shift. Although typically this technique is used to obtain circular polarization from linearly polarized elements, it can also be used with circularly polarized elements to enhance the polarization characteristics [40]. Employing this technique results in the cancelling of cross polarized signal components out. Hence the cross pol is reduced considerably and as a result a much lower axial ratio bandwidth is obtained.
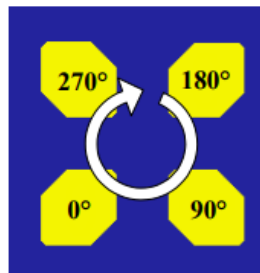
Figure 3.11: Sequential rotation [40]

3.4. Additive Manufacturing and Permittivity Profiles

Additive manufacturing is a process enabling creation of a physical product from a digital model, by means of depositing materials layer by layer. Recently additive manufacturing has received a great deal of attention in the development of RF components, specifically antenna elements [41]. The emergence of AM has facilitated a more efficient appoach in the production of DRAs. It aids in allowing greater flexibility in the design of DRAs. Moreover, it also enables rapid prototyping, allowing for faster iterations and testing of the designs. The most commonly used AM techniques include Fused Deposition Modeling (FDM) and StereoLithography (SLA). FDM used thermo filaments that are heated up at the nozzle to melt them. They are further deposited on a movable build platform, layer by layer. The build platform moves further downwards as each layer is deposited. SLA however uses quite a different approach where the build platform is immersed in a UV curable resin. This technique is based on the polymerization of this liquid mixture induced by UV light. The printing here is also done layer by layer where the build platform is moved as each layer is printed. The setups for both these additive manufacturing techniques are seen below.

(a) FDM Technique [42]   **(b)** SLA Technique [43]
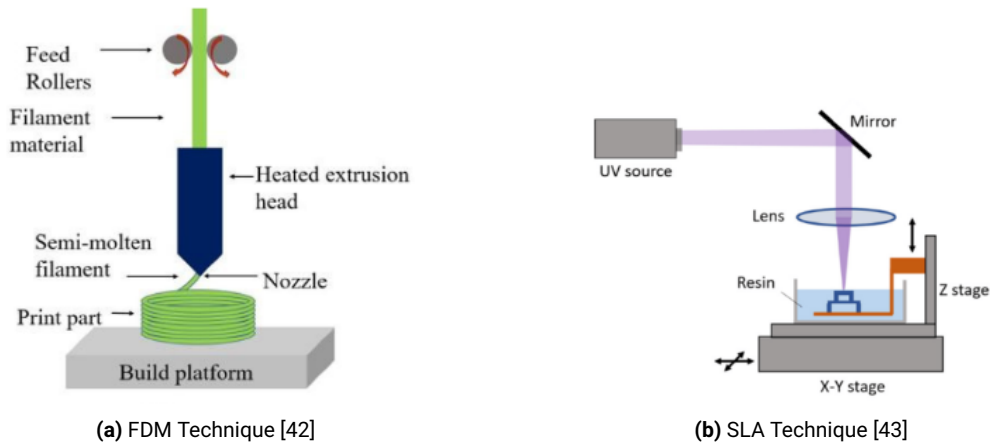
Figure 3.12: Popular AM setups

Due to the smaller layer thickness achievable by SLA, it enables a higher dimensional resolution, surface finish and accuracy as opposed to FDM [42]. Nevertheless, SLA is more expensive and yields products with lesser mechanical stability. However, an advantage of FDM that we are interested here it's capability to tailor the permittivity. This means it can produce a spatial variation of permittivity (vertically or radially) in the structure by volumetric infill percentage variations [44]. This potential of FDM to employ permittivity profiles in DRAs is made use of and further analyzed in this work, wherein various inhomogenous permittivity profiles are introduced and their benefits and impacts are studied.

4

Cylindrical DRA Model with and without Permittivity Profiles

In this chapter, the design considerations of the models are discussed. The performance characteristics that are primarily studied are also explained. First the design at a single element level is discussed and further extended to an array environment. The investigations into the benefits of employing a permittivity profile are carried out on CST Studio Suite, a high performance electromagnetic field simulation software used for the design, analyses and optimization of EM components and systems. The designs of DRAs with varied types of permittivity profiles are also detailed in this chapter.

4.1. Design Flow

The design flow followed is entailed below:

```
Choosing the resonant    →    Decide on the DRA    →    Employing design         →    Implementing the design
frequency                     (range of) permittivity    equations to get a            on CST Microwave Studio
                                                         preliminary estimate of
                                                         the parameters
                                                                                              │
                                                                                              ↓
Design of homogeneous    ←    Final design         ←    Update design based on   ←    Running parametric
permittivity DRA (same        (with permittivity        results from parametric        sweeps to optimize
physical dimensions)          profile)                  sweeps                         performance at required
and subsequent                                                                         frequency
comparative analysis
```

Figure 4.1: DRA design flow

Initially, the operating frequency is chosen. In this case as we are interested in the Ka band for Satcom applications, a centre frequency of 30 GHz is chosen. The permittivity range available for fabrication was 3 to 13.7. Based on this, the ϵ_r range was chosen to be 3 to 8, that is $\epsilon_{r,min}$ = 3 and $\epsilon_{r,max}$ = 8. A lower end of the range was chosen such that the size of the DRA can be increased while maintaining the same operational band. This is keeping fabrication at later stages in mind. Now preliminary calculations are done based on the design equations such that the desired modes are excited at the required frequency of operation. Using these as a starting point, a model is designed on CST and parametric analyses of the primary parameters are carried out.

Two types of feeding are investigated in this work. Initially a dual probe fed design is used to investigate the benefits of the permittivity profile. This is done with the purpose of drawing the focus to permittivity profiles and understanding how coupling is affected in dual port systems. Moreover, a dual probe feeding provides better axial ratio as opposed to cross slots. However, due to fabrication constraints, the realization of the probes of small radius embedded in the DRA becomes cumbersome. Therefore an aperture fed model is designed as it can be fabricated relatively easily. This is demonstrated for single linear polarization in Section 5.6.

The initial model with probes is such that the DRA with the permittivity profile is placed on a ground plane, with probes embedded in the DR. The parameters analyzed include the radius of the DRA (a), height of the DRA (h), height of the probe (h_{feed}), radius of the feed (r_{feed}) and the position of the probe in the DR (a_{pos}). Now based on results from the parametric sweeps, the model is updated to obtain the desired performance. After multiple iterations of optimization, a final model is obtained. The settings used and the details of the various models are detailed in the following section.

4.2. Simulation Setup

CST Microwave Studio is employed for all analyses, with time and frequency domain solvers used for single element and array simulations respectively. The time domain solver is a 3D full-wave solver which integrates both finite integration technique and transmission line matrix in a single package. The frequency domain solver is based on the finite element method and can calculate all ports at the same time making it efficient for simulation of multi port systems like arrays.

The design procedure is carried out at a single element level initially by executing parametric sweeps and optimizing the parameters to arrive at the required operational band. Initially, for the purpose of analysis a dual probe fed cylindrical DRA with a vertical permittivity profile is designed. As the definition of an inhomogeneous material is not possible on CST, such a profile is realized by means of discrete shells or layers of homogeneous dielectric material. This forms an approximate for the desired permittivity profile in the DRA. The number of shells (N) is kept at 10. Simulations were carried out with 20 layers but yielded similar results as $N = 10$. Hence N was chosen as 10 to reduce simulation times. Now considering the total

height of the CDRA to be h, the height of each layer will then be h/N mm. Let the maximum and minimum values of the permittivity range be $\epsilon_{r,max}$ and $\epsilon_{r,min}$ respectively. Thus we arrive at the permittivity of the nth layer here, which is

$$\epsilon_{r,n} = \epsilon_{r,(n-1)} + \frac{\epsilon_{r,max} - \epsilon_{r,min}}{N} \qquad (4.1)$$

Based on the material available for fabrication, the range of permittivities was chosen from 3 to 8. The realization of a vertically increasing permittivity profile can be visualized in the figure below.
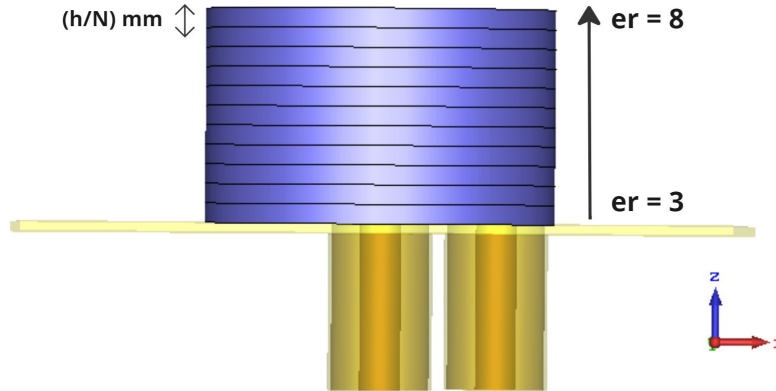
Figure 4.2: Vertical Permittivity profile realization on CST

The CDRA is mounted on a ground plane and fed by means of two probes embedded in the DR. Better coupling of the probes to the DR was observed on moving them inside the dielectric resonator, hence the same design choice was made. The dual probe configuration enables the DRA to operate in circular polarization by applying a 90° phase shift between the ports as shown in Figure 4.4. Port 1 is kept at 0° and Port 2 at 90° to generate right hand circular polarization. Conversely, LHCP can be obtained by switching the phase of both the ports (Port 1 at 90° and port 2 at 0°). Waveguide ports in CST are used for the purpose of excitation such that the port covers the entire cross-section of the coax. The fundamental mode of the coaxial cable is considered where the electric fields move from the inner to outer conductor. The port is defined on CST as shown below in Figure 4.3
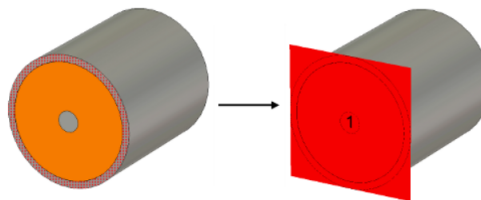
Figure 4.3: Coax on CST
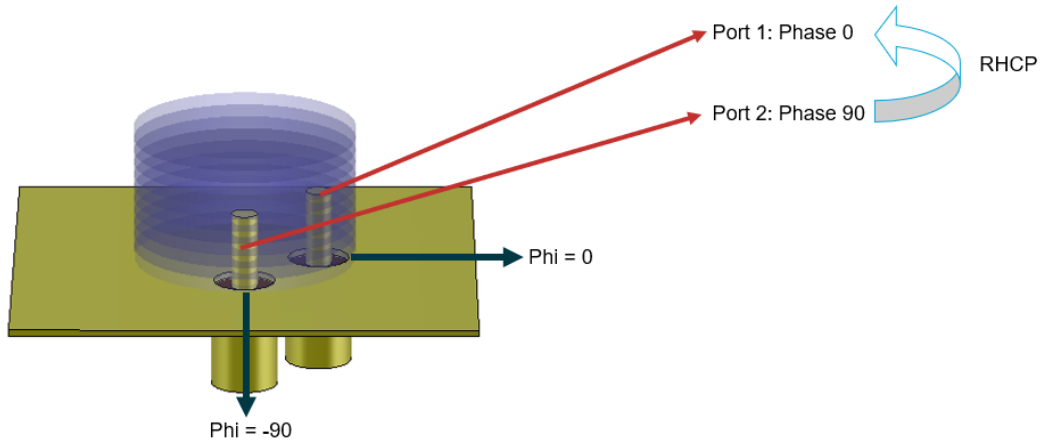
Figure 4.4: Dual probe configuration

Now the top and side views of the model are visualized, where all the parameters are shown. Keeping the permittivity profile constant, the radius (a) and the height (h) play a crucial role in deciding the operating frequency band. The coupling of the feed to the DR is primarily affected by the position of the probe from the centre (a_{pos}) and the height of the probe above the ground plane (h_{feed}).

(a) Top view   **(b)** Side View
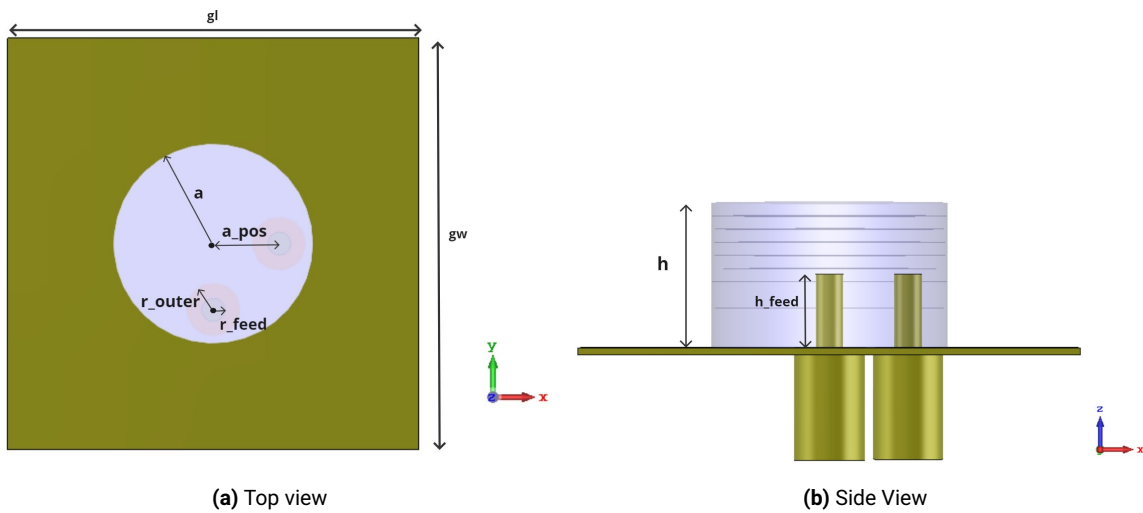
The general parameter values are decided based on the results from parametric sweeps and these are further fine tuned to obtain the required performance for analysis. The increase in effective permittivity and radius of the CDRA was generally seen to decrease the resonant frequency. The increase in height resulted in more resonances across the frequency scale, due to the excitation of higher order modes in the resonating structure. The reflections from the ports were observed to decrease with increase in the probe height till a certain point, after which it increased. Hence it was a primary parameter as it affected the impedance matching. The parameter values are enlisted in Table 4.1.

Parameter	Description	Value (mm)
a	Radius of CDRA	1.8
h	Height of CDRA	2.2
r_{feed}	Probe radius	0.21
h_{feed}	Probe height above ground plane	1.11
r_{outer}	Probe outer conductor radius	0.5
a_{pos}	Probe displacement from DRA centre	1.2
gl	Ground plane length	7.5
gw	Ground plane width	7.5
gt	Ground thickness	0.1

Table 4.1: CDRA design parameters

Now using similar design techniques, various other permittivity profiles are also introduced. These include vertically decreasing, radially increasing, radially decreasing and a vertical profile that increases from ϵ_{min} to ϵ_{max} and then decreases back to ϵ_{min}. The choice of such profiles is to investigate and study the impact of linear and non linear profiles, and how well fields are confined within them upon excitation. It also enables us to look into the field distribution and consequent performances when the maximum permittivity is at different points in the DR geometry. The radial profiles are realized by means of concentric shells around one another. In all the cases, the number of layers/shells are kept at 10. These profiles can further be viewed in the following figures. The performance comparison of the utilization of the above mentioned profiles are further discussed in the next chapter.

(a) Vertically decreasing permittivity profile

(b) Non linear vertical profile
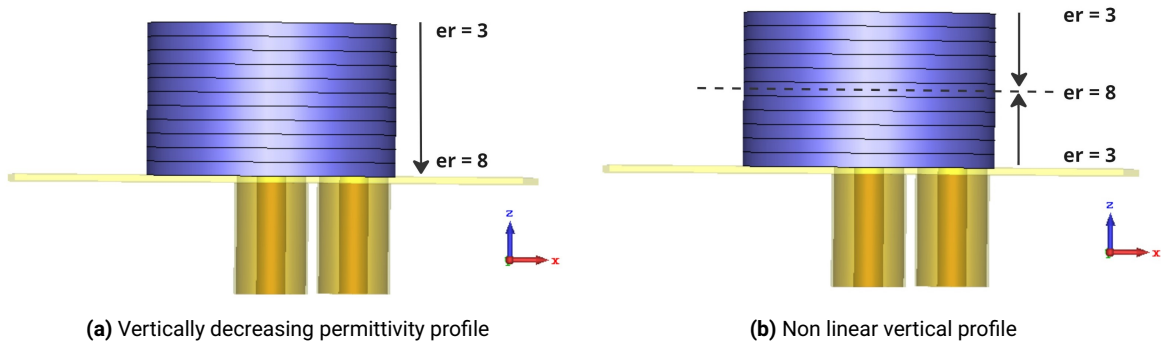
Figure 4.6: Vertically varying profiles

A more complex profile was also investigated, where the inner shell (with roughly half the radius) of the cylinder had a vertically varying profile. The shells around this layer was incorporated with a radially varying profile. The vertical profile is denoted in orange whereas the radial is in purple (Figure 4.8).

Now to fully study and understand the benefits of using these profiles, comparisons are drawn with a benchmark model without a profile. To ensure a fair comparison, this model is designed keeping all the dimensions the same. The permittivity is then chosen such that the performance is obtained over a similar frequency band as the other cases. Keeping this in mind, the permittivity is chosen as ϵ_r = 6.5 (Figure 4.9).

(a) Radially increasing profile (from centre)

(b) Radially decreasing profile (from centre)
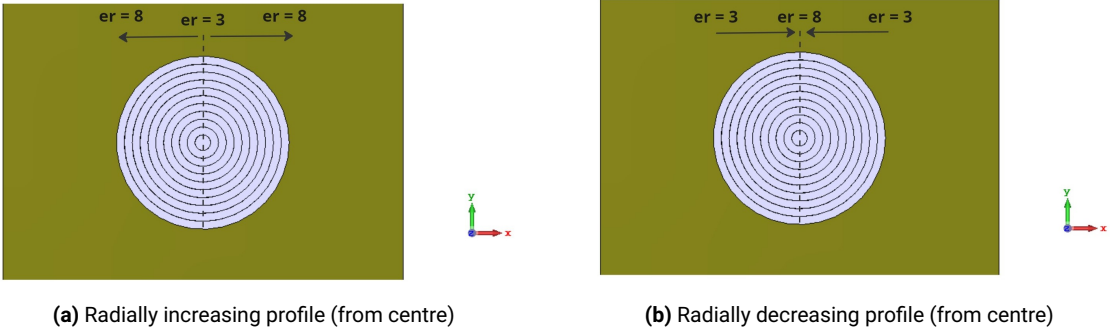
Figure 4.7: Radially varying profiles

(a) Vertical + radial profile (side view)

(b) Vertical + radial profile (top view)
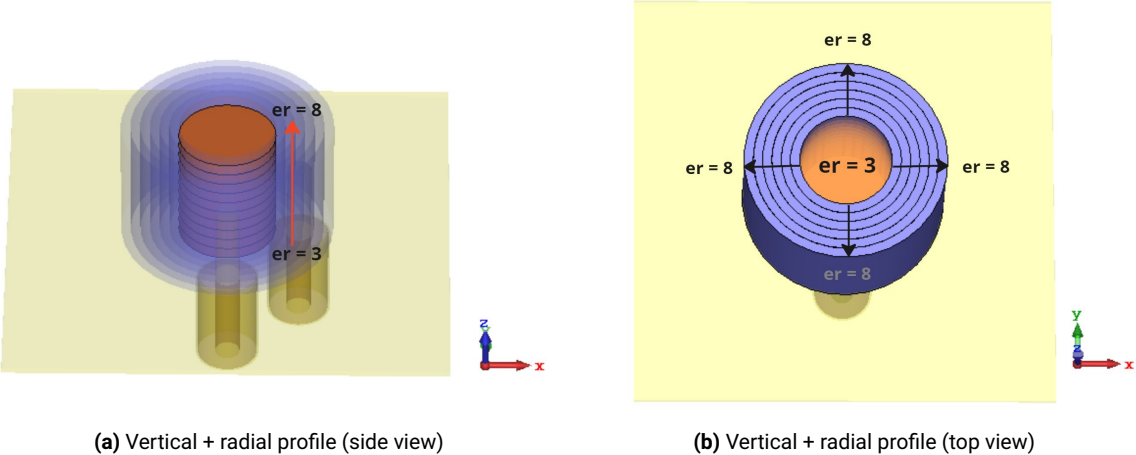
Figure 4.8: Vertical + radial inhomogeneous profile
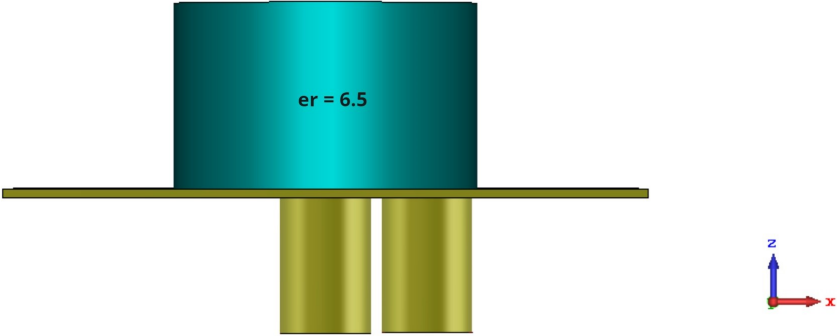
Figure 4.9: Model without tailored permittivity

The sequential rotation technique is illustrated further by modelling a 2x2 sub array where each element is rotated by 90° in the clockwise direction. The corresponding phase shifts are applied to the two ports and these are denoted by arrows in the figure below.
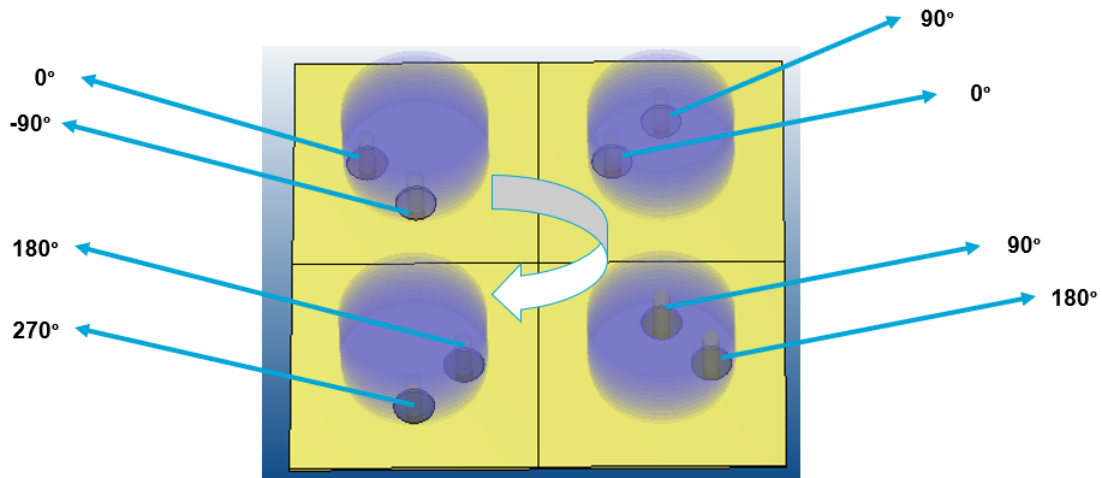
Figure 4.10: Sequentially rotated sub array

The single element models are extended to planar arrays to investigate the matching of the edge elements and mutual coupling effects between the probes within the same element and also adjacent elements. A model of a 3x3 array with unit elements having tailored permittivity can be viewed below.
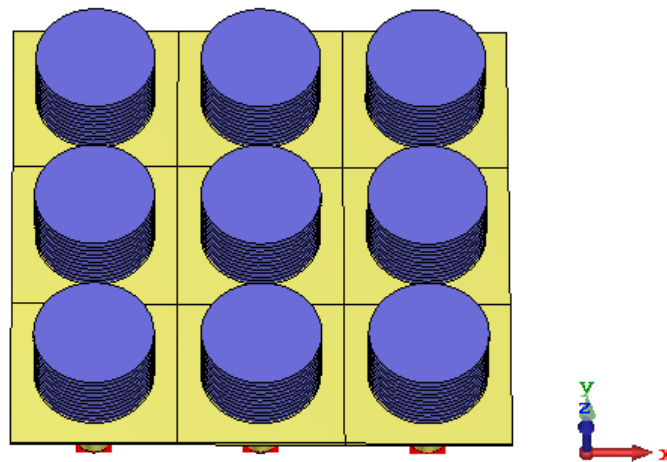
Figure 4.11: 3x3 array

To improve the matching of the edge elements, dummy elements were introduced around the array of elements with a homogeneous permittivity. Such elements are placed around the edge of the array and are not excited while in operation. This enables the reduction of spurious radiation of the edge elements in an array. These are highlighted in the figure shown below.
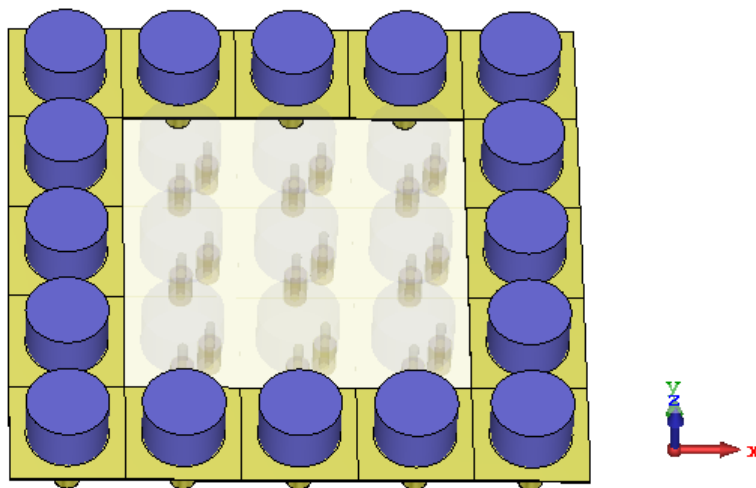
Figure 4.12: 3x3 array with dummy elements

As previously motivated, for fabrication purposes and measurements, a slot fed CDRA is designed. The dimensions are shown in Table 4.2. The primary differences from the previous models are enlisted below:

- Feeding changed to slot fed, as the dimensions of the pins from the previous models are too small to be realized successfully with the available fabrication techniques.
- Single linear polarization is realized, as using a cross slot results in a worse axial ratio. Moreover, as this is a proof of concept demonstrating the fabrication of an mm-wave DRA with tailored permittivity, LP is maintained.
- The permittivity range is shifted such that ϵ_{min} = 3 and ϵ_{max} = 7. Moreover, the operating frequency band is shifted to the satcom downlink frequency band (17.7 - 21.1 GHz), by increasing the primary dimensions such as height and radius. This is done to ensure easier and more effective fabrication.
- Holders (depicted in green) are introduced such that the DRA element can be secured firmly over the slot by screwing them into the substrate. This helps avoid use of glue while placing the element over the slot. The substrate used for simulations is Rogers RT5880 which has a permittivity of 2.2.

The dimensions of the slot play an important role when it comes to the coupling of the fields from the slot to the DR. Another crucial parameter that affects the coupling and also the matching is the extension of the microstrip line beyond the slot. These are depicted in the figures of the model as viewed in Figure 4.13.

Parameter	Description	Value (mm)
a	Radius of CDRA	3.2
h	Height of CDRA	8
$slotl$	Slot length	7
$slotw$	Slot width	0.45
ext	Extension of the microstrip line beyond the slot	3.75
$microw$	Microstrip width	1.5
dh	Substrate thickness	0.5
dl	Substrate length	8
dw	Substrate width	8
h_{ext}	Extension of holder into DR	1

Table 4.2: Dimensions of the slot-fed CDRA

(a) Side view

(b) Bottom view
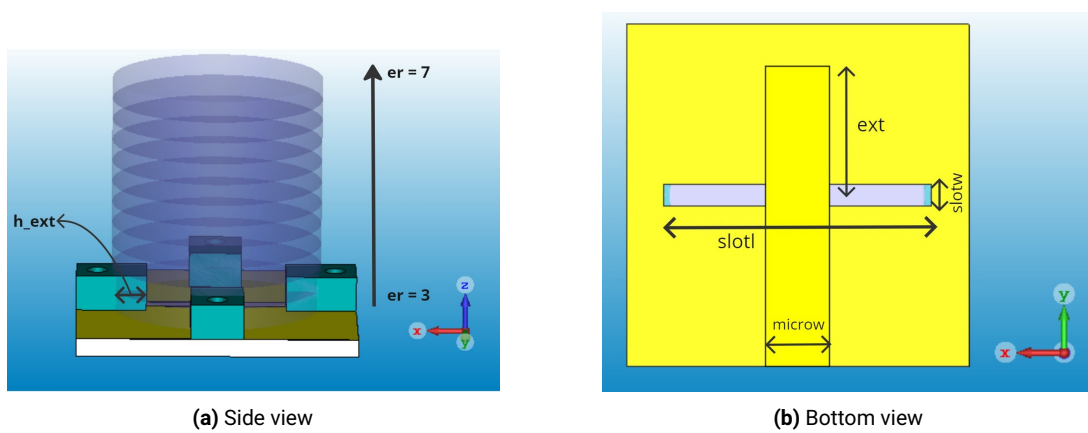
Figure 4.13: Slot fed CDRA

A single element of homogeneous permittivity with the same dimensions is also designed where the permittivity is defined as 5.5 to keep the operational band similar. This enables for an easier and a more fair comparison which studying the benefits of tailored permittivity. These single elements are then extended to a 1x9 linear array for comparison purposes. The choice to go with a linear array is made as the available connectors had a larger footprint, leading to connector overlap on being used in a planar array environment. The simulation model of such an array is shown in the figure below.
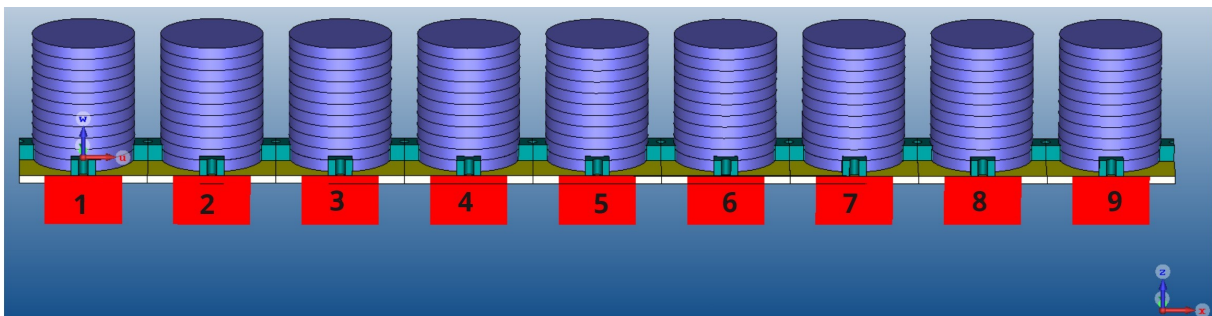
Figure 4.14: Slot fed 1x9 array

5
Results and Analysis

In this chapter, we dive into the results from simulations of the models that were explained in the previous chapter. The performance criteria are discussed first, followed by the presentation of the results and further analysis of these results. The comparison of the various permittivity profiles are carried out, the best performing one is then compared with the model having a homogeneous permittivity. The results of sequential rotation are then presented. These are succeeded by the analysis of the array performance of the unit elements. This also includes the incorporation of dummy elements where improvement in the matching of edge elements in shown. Finally, the simulation results of the slot fed model designed for fabrication are analyzed.

5.1. Performance Criteria

The performance metrics studied for the analysis of the models are entailed in this section. At a single element level, the metrics of interest are the bandwidth, far field pattern, realized gain, cross polarization, axial ratio bandwidth and the coupling between the ports in a dual port configuration.

Far fields can be plotted in 2D on a u-v plane with color depicting the intensity of the electric field at any point. U and V here are one dimensional projections of the angular space with $u = sin\theta.cos\phi$ and $v = sin\theta.sin\phi$.

Antenna gain is an important figure of merit that describes the performance of an antenna. Although the gain takes into consideration the losses of the antenna element like conduction and dielectric losses, it does not take into account the mismatch (reflections) losses when the antenna is connected to a transmission line. Hence we use realized gain which also incorporates the reflection losses in it. Gain and realized gain are expressed in dB although they are dimensionless quantities.

Another primary metric that we consider here is the impedance bandwidth. This is defined as the operating band of the antenna, that is the frequency range where the reflections from the ports fall below -10 dB. The input impedance and radiation efficiency are related to the impedance bandwidth. It can be expressed as the percentage of the difference between the maximum and minimum frequency over the centre frequency.

$$BW = \frac{f_{max} - f_{min}}{f_0} \cdot 100\% \tag{5.1}$$

In a dual probe configuration that we use for the simulations, the coupling between the ports is also a noteworthy metric that defines the overall performance while operating in CP. The reflections from the second port while the first one is excited (S2,1) is analyzed.

From the far field patterns, the polarization at every point on radiation sphere can be resolved into two orthogonal components, namely co-polarization and cross-polarization. The former denotes the polarization that the antenna is intended to radiate or receive while the latter is the redundant orthogonal component. It is desired to have a cross polarization much below the co-polarization. Axial ratio is characteristic defining the performance of circularly polarized antennas. It is defined as the ratio of the major and minor axes of elliptical polarization. The axial ratio bandwidth is defined as the range of frequencies where it drops below 3 dB.

In an array environment we are primarily interested in the mutual coupling between the elements and the range of scanning the array can achieve. Mutual coupling is the electromagnetic interactions between the elements in an array. The current generated and impedance of each element in an array is defined by its own excitation as well as the contribution of the neighbouring elements. It is inversely proportional to the spacing between the elements. Scanning in an array can be achieved by progressively varying the phase shift between the elements. Such arrays are called phased arrays where phase shifters are used to provide the necessary phase shifts to the elements. Linear arrays are capable of scanning only in a single plane, but planar or 2D arrays can deflect the beam in both the planes (θ and ϕ). For a planar array, the progressive phase shifts in the x and y axes can be obtained from the expressions:

$$\beta_x = kd_x sin\theta cos\phi \tag{5.2}$$

$$\beta_y = kd_y sin\theta sin\phi \tag{5.3}$$

where $k = 2\pi/\lambda$ is the propagation constant, d_x and d_y are the element spacing in the x and y directions respectively and θ, ϕ are the required scan angles.

5.2. Comparison of permittivity profiles

The numerous permittivity profiles detailed in chapter 3 are analyzed here. Initially the ports are excited individually to study the reflections from the other port (coupling). Subsequently, both the ports are excited such that the antenna element operates in CP. This enables the analysis and comparison of the cross polarization and axial ratio bandwidths for all the cases. After viewing the results, a comparison table is made enlisting the primary performance metrics

considered. The profiles are labelled as follows:

Name	Definition
Profile 1	Vertically increasing [Figure 4.2]
Profile 2	Vertically decreasing [Figure 4.6a]
Profile 3	Radially increasing [Figure 4.7a]
Profile 4	Radially decreasing [Figure 4.7b]
Profile 5	Non linear profile [Figure 4.6b]
Profile 6	Vertical + radial profile [Figure 4.8]

Table 5.1: Permittivity Profile Details

To begin, one port is excited, and the S1,1 and S2,1 plots are provided (Figures 5.1, 5.2) to investigate the impedance bandwidth and port coupling.
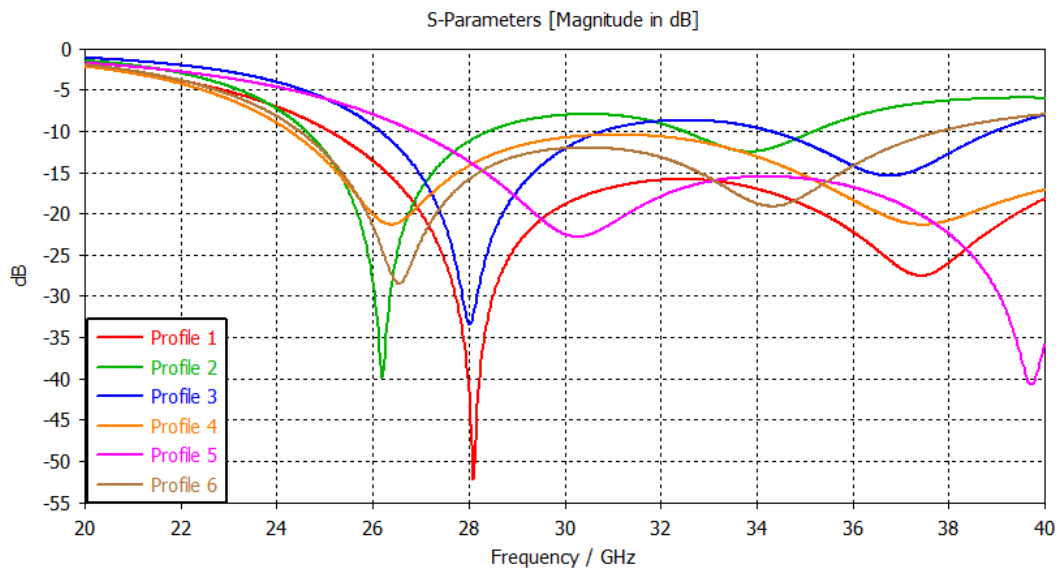
Figure 5.1: S1,1 Curves for different permittivity profiles (single element level, dual coax fed)

The impedance bandwidths obtained from the plots are enlisted in the following page. For cases where the reflections are below -10 dB even beyond the simulated frequency range of 40 GHz, the upper frequency limit f_{max} for calculating the fractional bandwidth is taken as the value where the gain is 3 dB lower than the maximum value (reduced to half). Hence the upper frequency limits for Profiles 1,4 and 5 are chosen accordingly. The fractional bandwidths are compared below, with the centre frequency as 30 GHz.

Profile	Impedance Bandwidth (%)
1	46.36
2	35.26
3	43
4	42.45
5	44.52
6	42.76

Table 5.2: Fractional Bandwidth Comparison

We observe that the design with a vertically decreasing profile has the smallest bandwidth (35.26%) among the models. Profile 1 is seen to have the largest bandwidth, around 46%. The non linear profile has slightly a lower bandwidth (1.8% lower) than profile 1, while that of profiles 4 and 6 are found to be comparable to each other.

Now we observe the reflections from the second port (coupling). The S2,1 curves for all the cases are shown below in a single plot for ease of comparison. The vertically decreasing profile (2) has the worst coupling of the group, increasing to as high -6 dB around 33 GHz. The radially ascending profile (3) is also observed to have an increased coupling reaching -6 dB but at a higher frequency of 38 GHz. The vertically ascending profile (1) is seen to perform best in terms of coupling as it is consistently low (below -8.5 dB) across the frequency band. The non linear profile (5) is also found to have a comparable coupling performance.
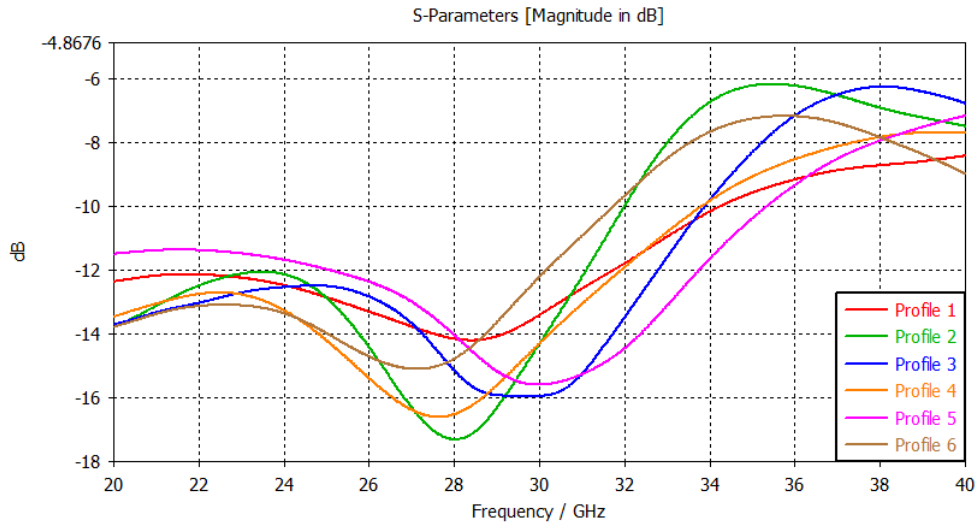
Figure 5.2: S2,1 Curves for different permittivity profiles (single element level, dual coax fed)

In the case of Profile 2, the permittivity decreases as we move upwards, leading to the electromagnetic fields being more concentrated (due to slower propagation at high permittivity regions) at the bottom of the DRA. As the probes are placed closer to the bottom, they are subjected to a higher field intensity, which results in higher coupling. Profile 6 results in complex electromagnetic field distributions due to the differing permittivity gradients. As the

probes are positioned in areas where these fields overlap significantly, relatively high coupling is observed. This is due to the vertical gradient trying to confine the fields towards the top, while the radial gradient is attempting to confine them near the outer wall. Upon analyzing Profile 3, it concentrates the electromagnetic fields towards the outer wall of the DRA. The field intensities around the probes due to their proximity to the outer wall. Hence they are subjected to relatively high field densities, resulting in intermediate levels of coupling. The fields in Profile 4 are concentrated more towards the center of the DRA. As the probes are not located at the center, the field intensity around them is less, leading to lower coupling. The configuration with Profile 5 increases the field confinement in the middle region. Given that the probes are located closer to the walls and the probe height is slightly below the middle, where permittivity is high, the coupling is reduced. Now looking into Profile 1, the electromagnetic fields are confined towards the top of the DRA due to increasing permittivity. Since the probes are not extending to the top, the field intensity around them would be less, resulting in the lowest coupling among the profiles.

The excitation of port 1 results in the CDRA operating in horizontal polarization. That is, the co-polarization here is horizontal and cross-polarization is vertical. These are shown in the uv plots below. Furthermore, a table summarizing the maximum co-pol and cross-pol values are also provided.
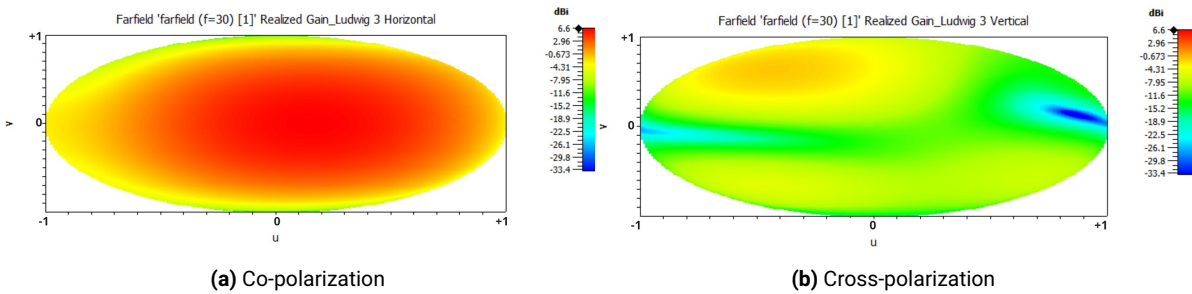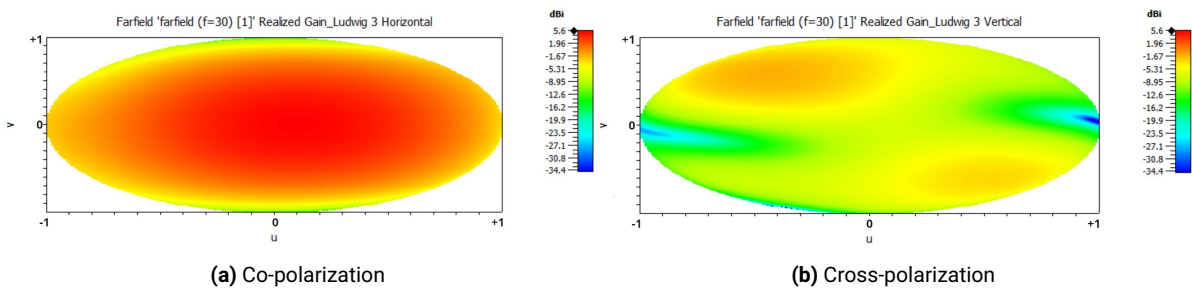
(a) Co-polarization

(b) Cross-polarization

Figure 5.3: Profile 1 (LP)

(a) Co-polarization

(b) Cross-polarization

Figure 5.4: Profile 2 (LP)

(a) Co-polarization   **(b)** Cross-polarization

Figure 5.5: Profile 3 (LP)

(a) Co-polarization   **(b)** Cross-polarization

Figure 5.6: Profile 4 (LP)

(a) Co-polarization   **(b)** Cross-polarization
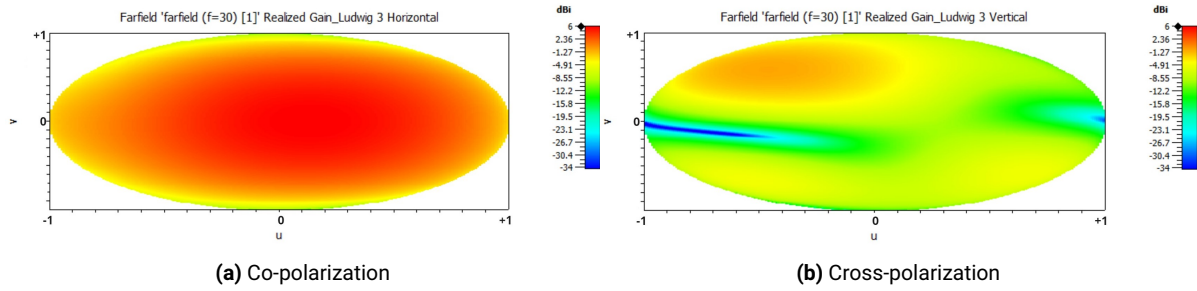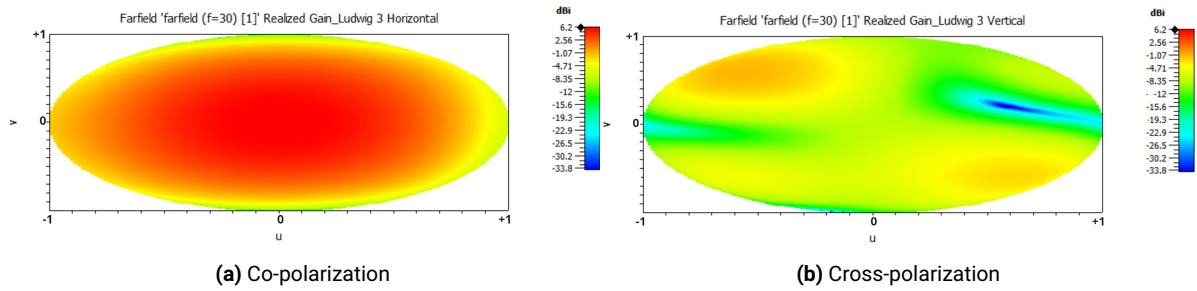
Figure 5.7: Profile 5 (LP)
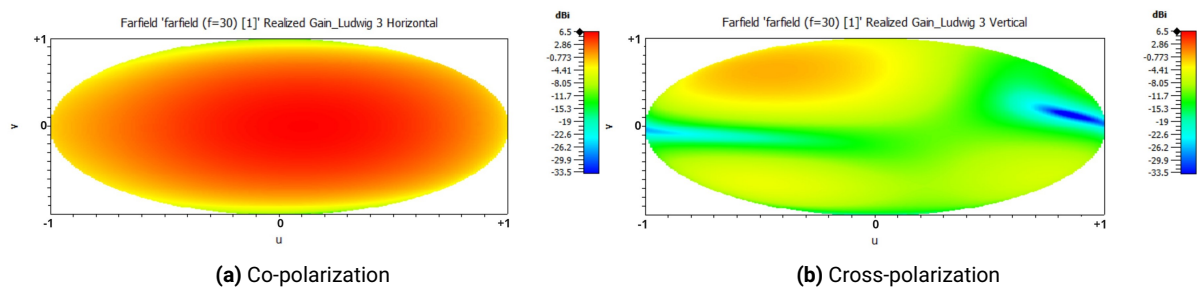
(a) Co-polarization   **(b)** Cross-polarization
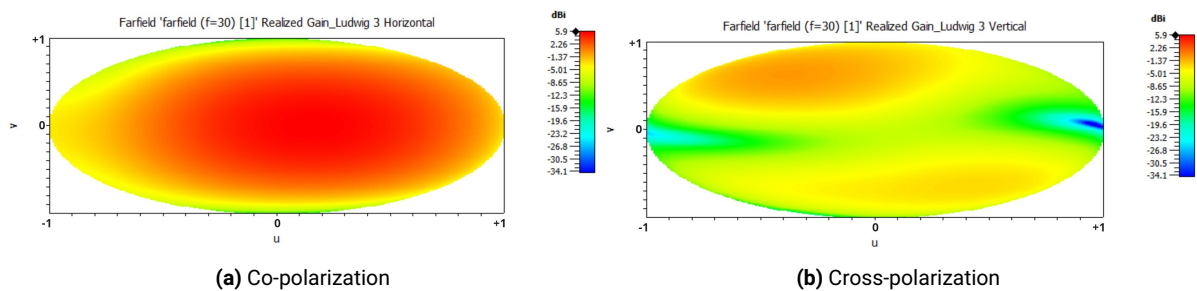
Figure 5.8: Profile 6 (LP)

Profile	Co-polarization (Horizontal) (dBi)	Cross polarization (Vertical) (dBi)
1	6.6	-1.05
2	5.6	-0.6
3	6	-0.53
4	6.2	-0.9
5	6.5	-0.86
6	5.9	-0.44

Table 5.3: Realized gain comparisons (max values)

Now we observe the performance when the CDRA is operated in circular polarization. In order to generate circular polarization, the ports are excited simultaneously with a 90° phase shift between them. The active S parameters of the port without the phase shift (port 1 here) is observed to check the impedance bandwidth under CP operation.
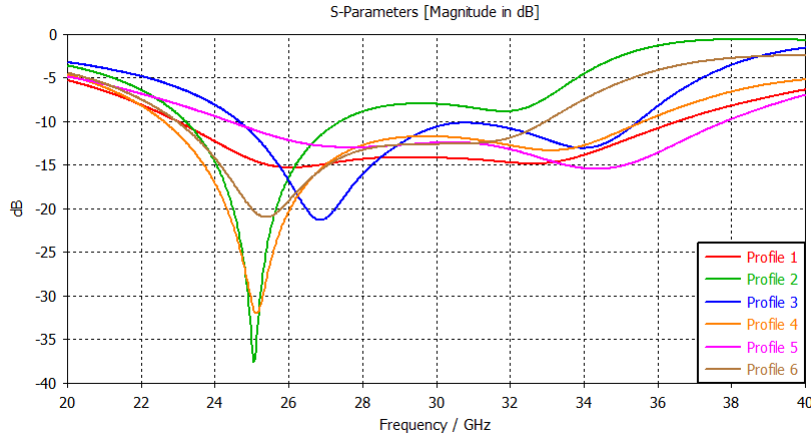
Figure 5.9: S1 (CP operation) for different permittivity profiles (single element level, dual coax fed)

Profile	Impedance Bandwidth (%) [Dual port excitation]
1	45.28
2	-
3	36.06
4	43.39
5	44.92
6	33.35

Table 5.4: Fractional Bandwidth Comparison (Port 1)

Here we observe that in the case of profile 2, the matching is lost over the frequency band upon CP operation. So far we can conclude that it is the worst performing of all the models. Profile 1 performs the best with a high impedance bandwidth of 45.28%, although the non linear profile performs quite similar to it (only ∼0.36% lower). Therefore we consider profiles 1 and 5 as models of interest.

Now the active S parameters of port 2 for all the cases are visualized in the figure below. The reflections observed here for all the profiles follow a similar trend seen with the coupling between the probes as seen in Figure 5.2. Here we see that profile 5 better matches the active S parameters of the second port under CP operation, hence a better overall operational band is obtained in this case.
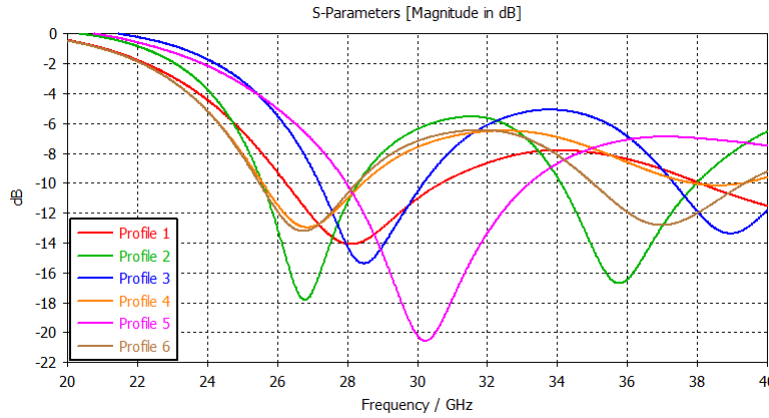
Figure 5.10: S2 (CP operation) for different permittivity profiles (single element level, dual coax fed)

Hereafter, we take a look at the co-polarized and cross-polarized components for the different cases under CP operation. As discussed before, the phase shifts are provided such that RHCP is obtained (looking into port 1). This implies that the co-polarized component is Right Circularly Polarized and the cross-polarized (redundant) component is Left Circularly Polarized. These components can be visualized in 2D by means of a uv plot. The realized gains at $\theta = 0°$ (broadside), for both the components are noted. The maximum co-pol and cross-pol values are further presented in a tabular form for ease of comparison.

The realized gain for co-pol is seen to be the lowest for profile 2 at 5.6 dBi. This can be attributed to the high coupling between the ports and consequent loss of matching over the band. Moreover, the same phenomena results in profile 6 having a similar gain of about 5.8 dBi. The radially descending profile (4) is found to have the highest gain of 6.7 dBi. The gains of profiles 1 and 5 are found to be almost equal at 6.52 and 6.44dB respectively.

The cross-pol is then observed to find that profiles 2 and 6 indeed have the highest values of -7.14dB. This can again be traced back to the high coupling between the ports in both the cases. Cross-pol values for all the other cases are below -8.1 dB, with the non linear profile having the lowest value of -9.82 dB. In general the relatively higher cross polarization arises due to the cylindrical geometry of the DR and the use of probe feeding.
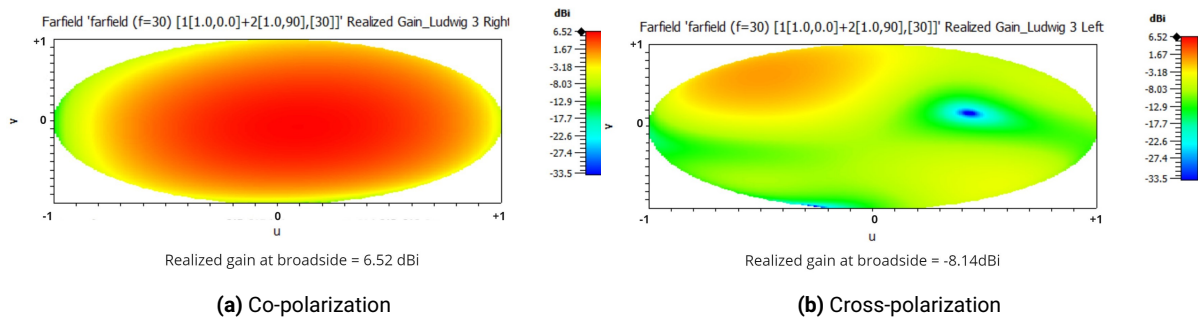
Realized gain at broadside = 6.52 dBi

(a) Co-polarization

Realized gain at broadside = -8.14dBi

(b) Cross-polarization

Figure 5.11: Profile 1 (CP)

(a) Co-polarization

(b) Cross-polarization

Figure 5.12: Profile 2 (CP)

(a) Co-polarization

(b) Cross-polarization

Figure 5.13: Profile 3 (CP)

(a) Co-polarization
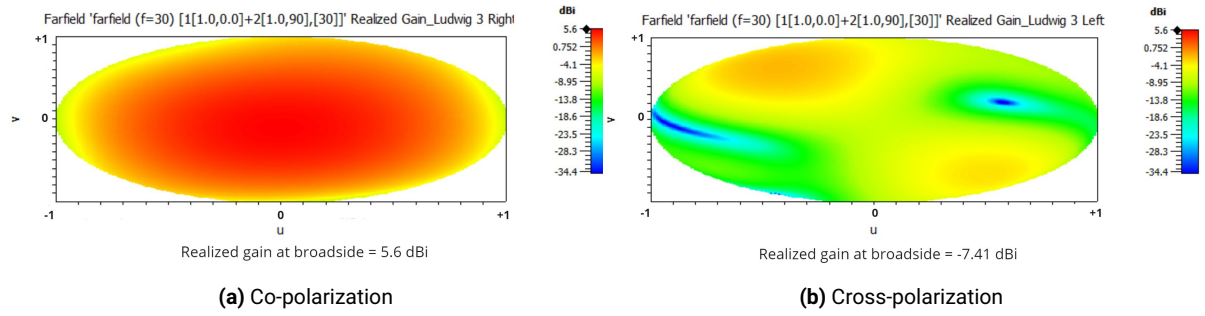
(b) Cross-polarization
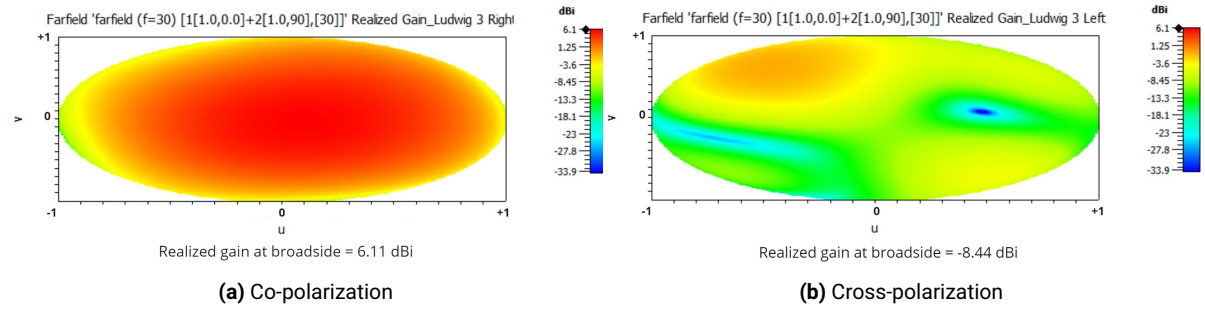
Figure 5.14: Profile 4 (CP)
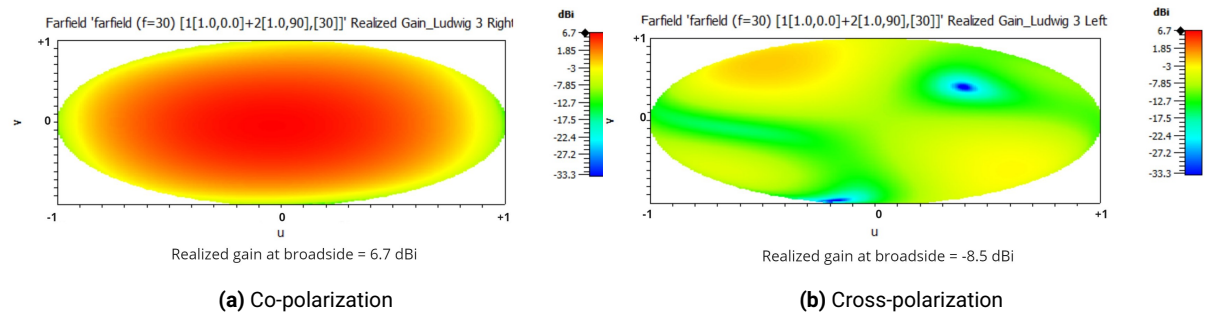
(a) Co-polarization

(b) Cross-polarization
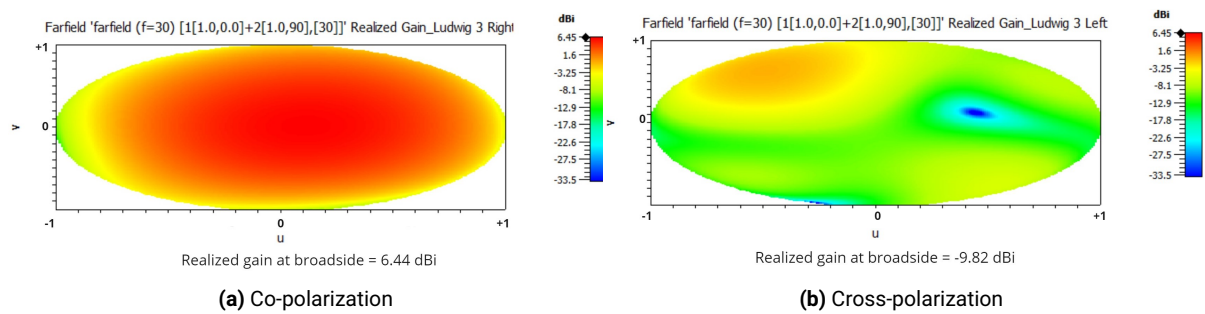
Figure 5.15: Profile 5 (CP)

Profile	Co-polarization (Right) (dBi)	Cross polarization (Left) (dBi)
1	6.52	-0.43
2	5.6	-0.74
3	6.11	-0.58
4	6.7	-0.9
5	6.44	-0.5
6	5.83	-0.29

Table 5.5: Realized gain comparisons (max values)

(a) Co-polarization

(b) Cross-polarization
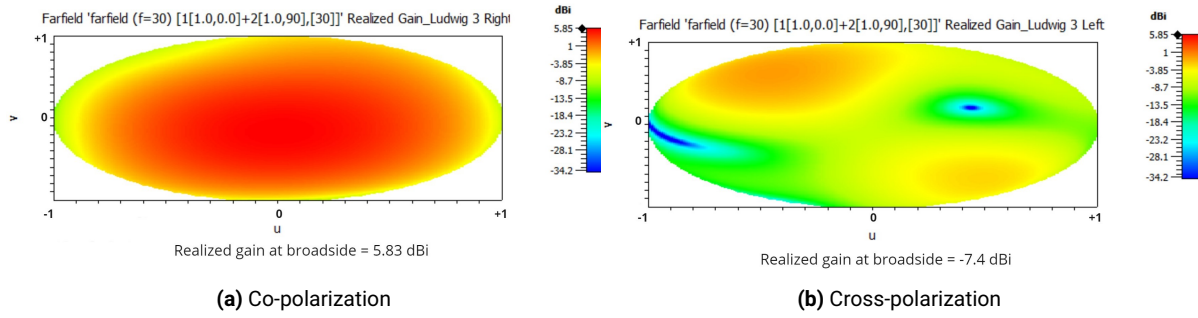
Figure 5.16: Profile 6 (CP)

The variation of gain across frequency is plotted on CST by utilizing post processing result templates. This change in gain is stable across the frequency band for all the designs (Figure 5.17). However, the peak gains for profiles 2, 3 and 6 are found to be the lowest, not crossing the 6.2 dB mark across the simulated frequency band. Again we see there that profiles 1 and 5 have similar gain vs frequency curves, where both attain a peak gain of around 6.8dB.
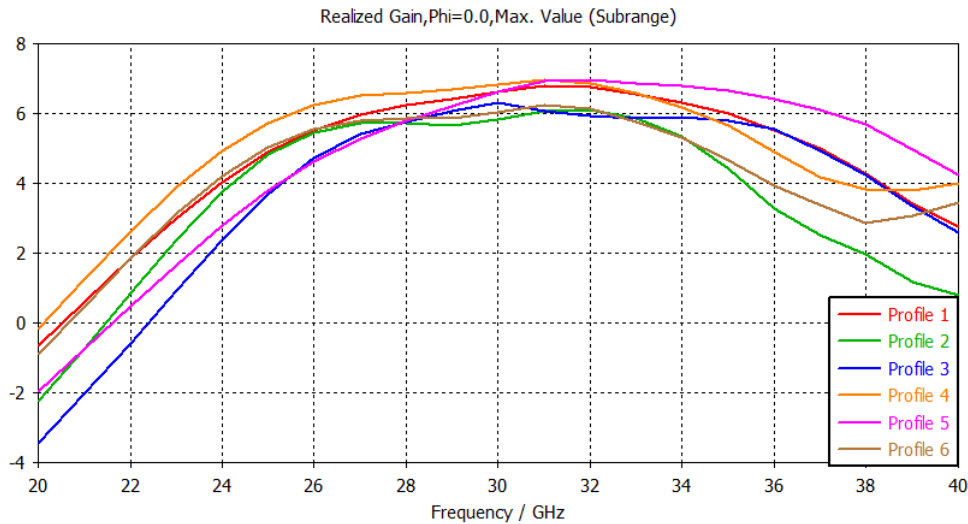
Figure 5.17: Gain vs Frequency for different permittivity profiles (single element level, dual coax fed)

Finally, we analyze the last performance metric of interest here, which is the axial ratio bandwidth. In literature, values of axial ratio below 3 dB are considered acceptable. Therefore the frequency range where the axial ratio falls below 3 dB is defined as the axial ratio bandwidth. As expected, the axial ratio of profile 2 is the highest and does not drop below 2.9 dB, because of which the AR bandwidth is not calculated. The vertically ascending profile (1) has the highest value of 25%. As expected, Profile 6 returns a smaller AR bandwidth of around 17%. The percentage values for the axial ratio bandwidths for all the models are compared in Table 5.6.
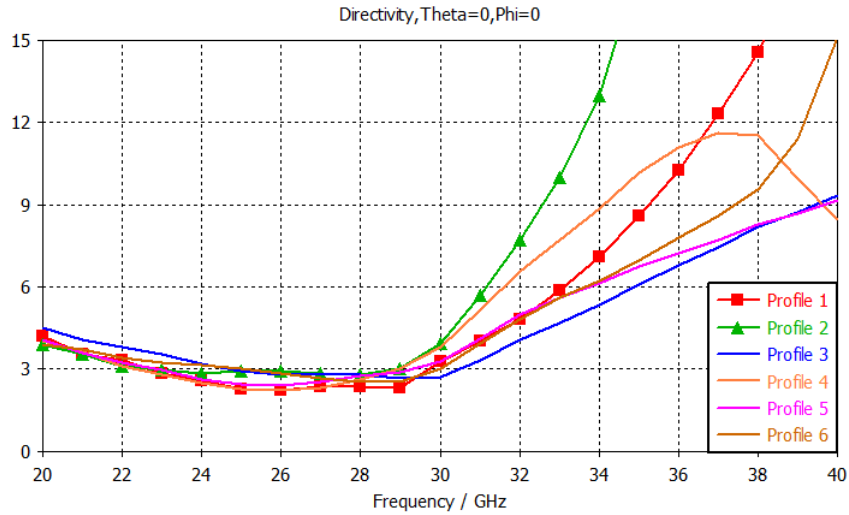
Figure 5.18: Axial Ratio vs Frequency for different permittivity profiles (single element level, dual coax fed)

Profile	3-dB Axial Ratio Bandwidth (%)
1	25
2	-
3	21.11
4	23.7
5	24.44
6	17.6

Table 5.6: Axial Ratio Bandwidth comparison (on broadside)

All the performance metrics of interest are inspected and a design is chosen for comparison with a benchmark design of single permittivity. Overall, Profiles 1 and 5 perform similar to each other, however Profile 1 returns a better impedance bandwidth ($\sim$ 2% more) under LP operation. This can be attributed to the more gradual transition of the wave impedance within the DR due to the vertically ascending profile, resulting in a better matching over the band. Nonetheless, Profile 5 provides improved matching of the active S parameters of the second port, resulting in an improvement in the overall operational band under CP operation. As the prototype for fabrication is also designed for LP operation, we use Profile 1 for subsequent comparative analysis. In the next section we compare the performance of this model (Profile 1) with a benchmark design of homogeneous permittivity (ϵ_r = 6.5).

5.3. Comparison with benchmark design (homogeneous permittivity)

Here we aim to highlight the benefits of tailored permittivity in DRAs. This is done by performing comparisons of a model incorporating Profile 1 (as motivated in the previous section) with a benchmark model of homogeneous permittivity of 6.5 (Figure 4.9). The choice of the permittivity value was motivated by the objective of achieving a comparable operating band for both

the cases. Furthermore, the dimensions of the CDRA are kept the same to ensure a fair comparison. Following the analyses, a comprehensive table enlisting all the performance criteria is provided.

The plots presented have curves overlaid in a single plot to make for a more intuitive comparison. Initially the S parameters on a single port (1) excitation is studied. The S1,1 and S2,1 curves for both the cases are presented below
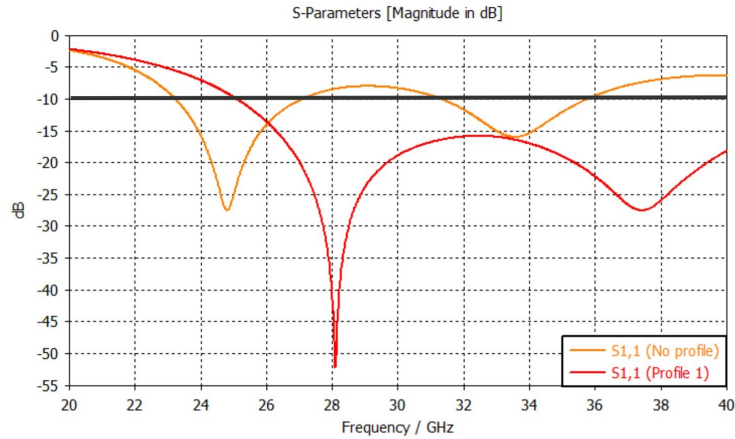
Figure 5.19: S1,1 curves (profile 1 vs homogeneous permittivity, single element, dual coax fed)
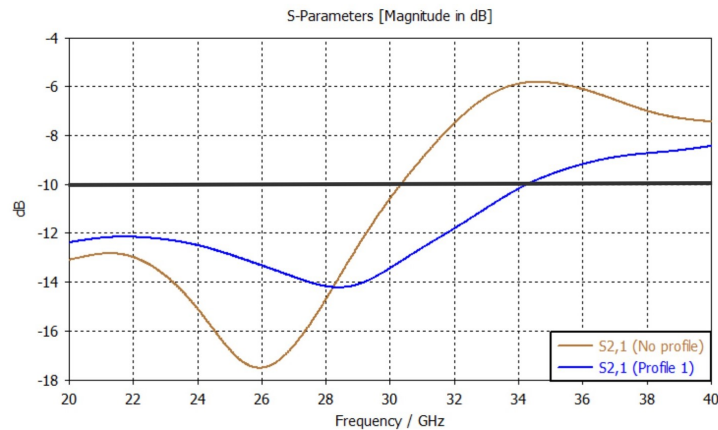
Figure 5.20: S2,1 curves (profile 1 vs homogeneous permittivity, single element, dual coax fed)

The results above clearly demonstrate the enhanced performance in the impedance bandwidth and coupling, achieved through the implementation of spatial variation of permittivity. The impedance bandwidth of the design with the vertical profile is at 46.36%, whereas the benchmark design returns a bandwidth of 39.2% which is $\sim$ 7% lower. In addition, the coupling performance displayed a significant advantage when compared to the single permittivity model. The coupling reaches as high as -6 dB for the benchmark model. On the contrary, the coupling is seen to be consistently below -8 dB. In case of the design without a profile, the fields within the DR are distributed more uniformly throughout whereas the profile allows for the tailoring of the field distribution resulting in lower coupling. This can be visualized from

the figure below, which shows the electric fields reaching port 2, depicted in arrows for both the models. The red circle around port 2 in both the figures encompass the fields reaching it and it is larger for the benchmark model as observed.

(a) Fields in Profile 1 model

(b) Fields in benchmark model
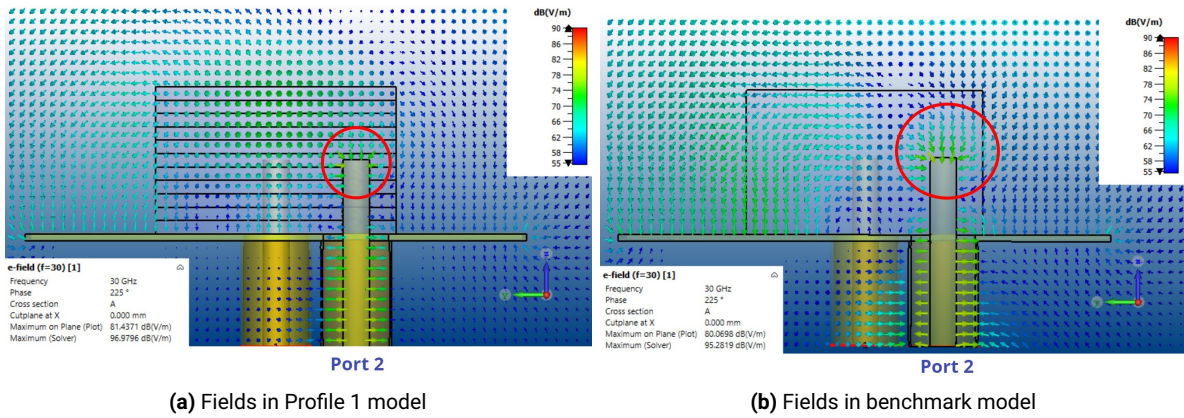
Figure 5.21: E fields (profile 1 vs homogeneous permittivity, single element, dual coax fed)

Now the models are operated in a CP configuration to primarily analyze the co-polarization, cross polarization and the axial ratio bandwidth. The impedance bandwidth of port 1 ($0°$ phase) under the simultaneous excitation of both the ports are examined (Figure 5.22a). We see that the bandwidth of the model without the profile is 33.06% which is around 12% lower than that of our model of interest here, which is at $\sim 45\%$ (mentioned in Table 5.4). The active S parameters of the second port is better matched upon using a profile (Figure 5.22b).

(a) S1 plot (CP operation)

(b) S2 plot (CP operation)
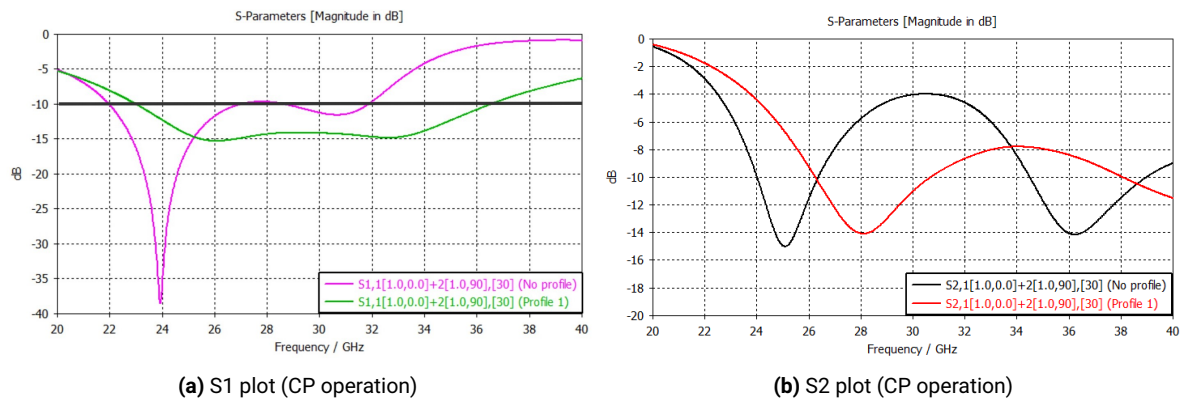
Figure 5.22: S1 and S2 curves (profile 1 vs homogeneous permittivity, single element, dual coax fed)

The 2D far fields plots are examined to analyze both the co polarization (right) and cross polarization (left) characteristics. These plots for the design with the profile 1 is presented in the previous section, in Figure 5.11. The uv plots shown below are of the benchmark model, where we see a reduced gain of 5.65 dBi (~ 1 dB lower) and a higher cross polarization level of -5.84 dBi at broadside, which is around 2.3 dB higher than that of the design that includes the profile.

The axial ratio is plotted against the frequency and then compared. We observe the AR bandwidth of the single permittivity model to be more narrow at 15.5%, which is about 10%

Realized gain at broadside = 5.65 dBi

(a) Co-polarization

Realized gain at broadside = -5.84 dBi

(b) Cross-polarization
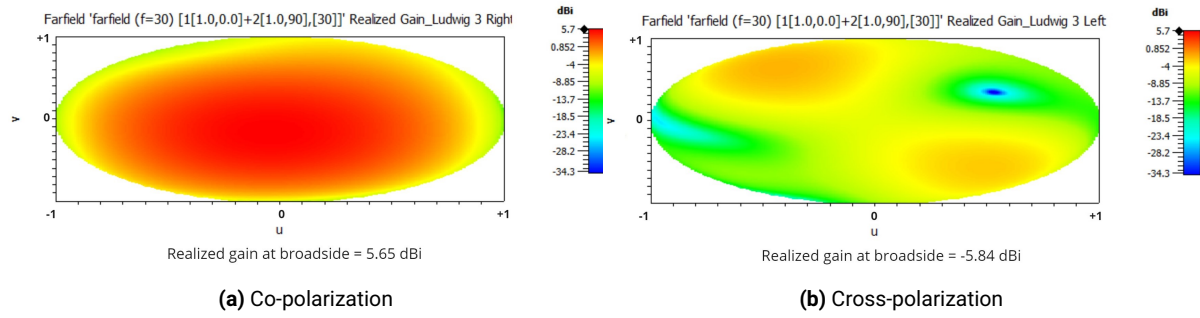
Figure 5.23: Co and cross polarization of benchmark model

lower than our model of interest. Moreover, the variation of gain with frequency is also noted, where we see that model with the vertical permittivity profile attains an overall higher peak gain across the operating band. The improvements in axial ratio and realized gain arise from the reduced coupling between the ports.
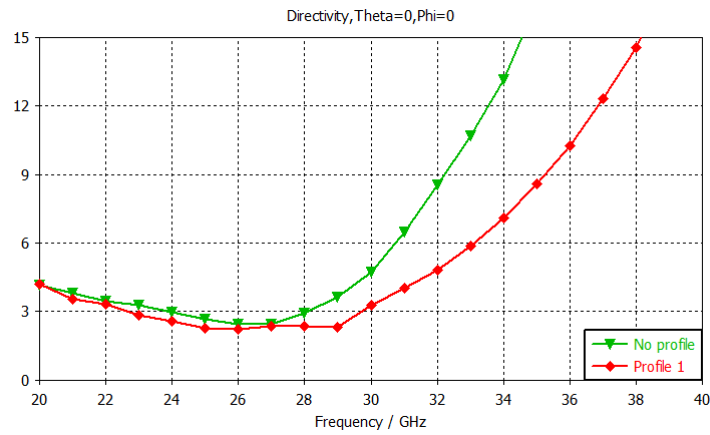
Figure 5.24: Axial Ratio comparison (profile 1 vs homogeneous permittivity, single element, dual coax fed)
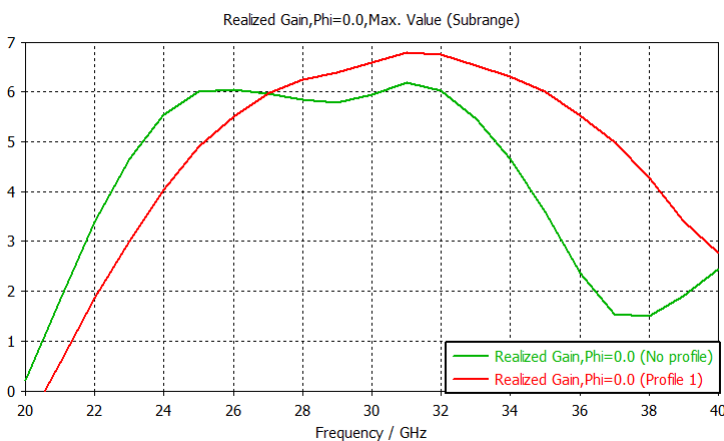
Figure 5.25: Gain vs Frequency comparison (profile 1 vs homogeneous permittivity, single element, dual coax fed)

A table summarizing the key observations from this section is presented below:

Performance metric	Model	
	Profile 1 (vertically ascending)	Benchmark model (ϵ_r = 6.5)
Impedance bandwidth (single port excitation) (%)	46.36	39.2
Impedance bandwidth (dual port excitation) (%)	45.28	33.06
Co-polarization (θ = 0) (dBi)	6.52	5.65
Cross polarization (θ = 0) (dBi)	-8.14	-5.84
Axial Ratio Bandwidth (%)	25	15.55

Table 5.7: Comparison of profile 1 with benchmark model

A subarray of four sequentially rotated elements with profile 1 is modelled (figure 4.10) further improve the cross polarization and the axial ratio of the single elements. Here we take a look at the metrics of interest, in Figures 5.26 and 5.27. We observe the cross polarization at broadside to have dropped significantly as seen below. Furthermore, the axial ratio bandwidth is enlarged with values falling far below 3 dB and reaching as low as 0 dB at 30 GHz signifying perfect CP operation. This is due to the cancelling of the cross polarized signal components brought about by such a configuration.
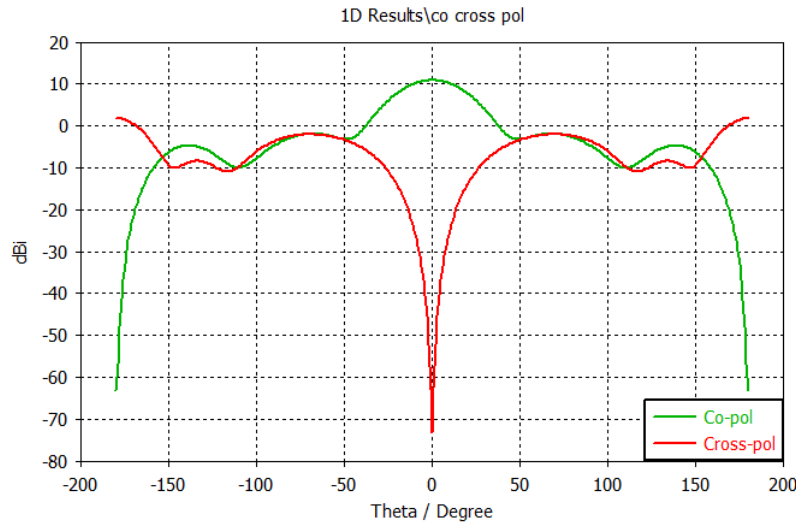
Figure 5.26: Co and Cross Polarization (Sequentially Rotated Subarray)
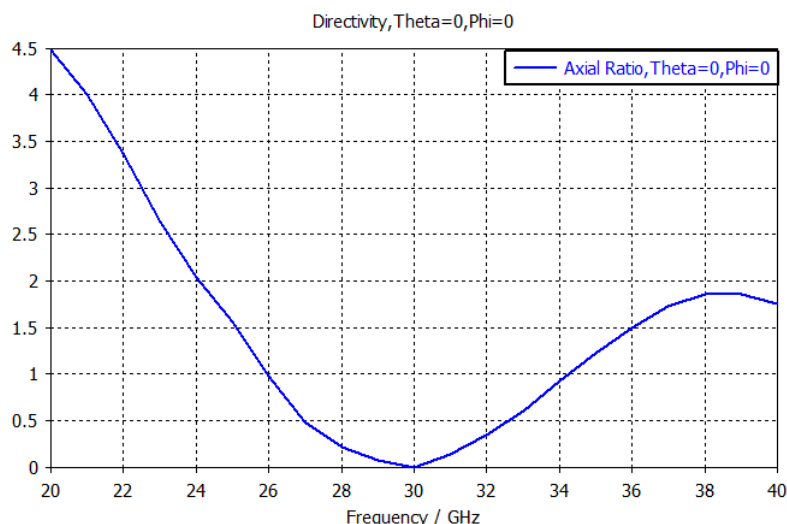
Figure 5.27: Axial Ratio (Sequentially Rotated Subarray)

5.4. Comparison of array performance (3x3)

Now we take a look at the array performance of both the models from the previous section by extending them to a 3x3 array. The spacing between the elements is kept at $\lambda/2$ at 30 GHz. Primarily, we look at the performance of the edge elements and the coupling between the ports in both the cases.

The ports are excited individually to analyze the matching of the centre and edge elements of the array. The reflections from the neighbouring ports (mutual coupling) are also observed. The port definitions can be visualized in the figure below.
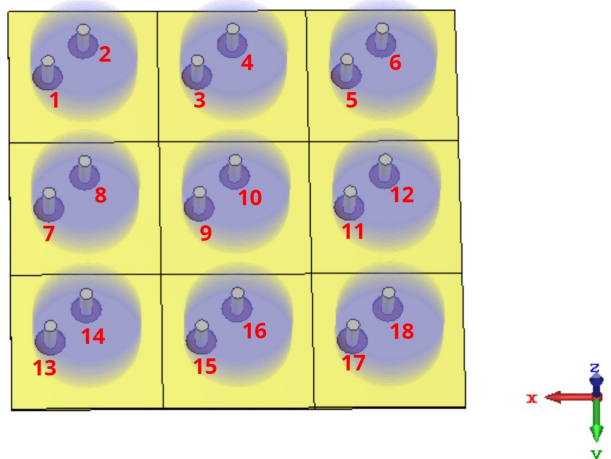
Figure 5.28: Port definitions for the array

First we look at the array with elements having a permittivity profile, where the S parameters of one of the ports from the centre element (9) and two edge elements (1, 17) are plotted below. We see that even in the case of edge elements, the matching is not lost over the operational frequency.
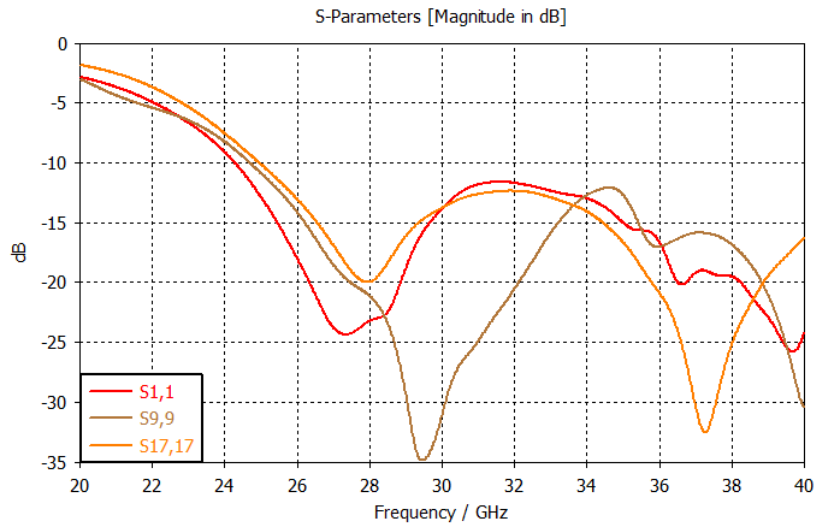
Figure 5.29: S parameters (3x3 array with profile, dual coax fed)

However, upon observing the same plots for the array environment with elements of homogeneous permittivity, we see the edge elements lose their matching. This can be attributed to the spurious radiation of the edge elements and is shown in the figure below.
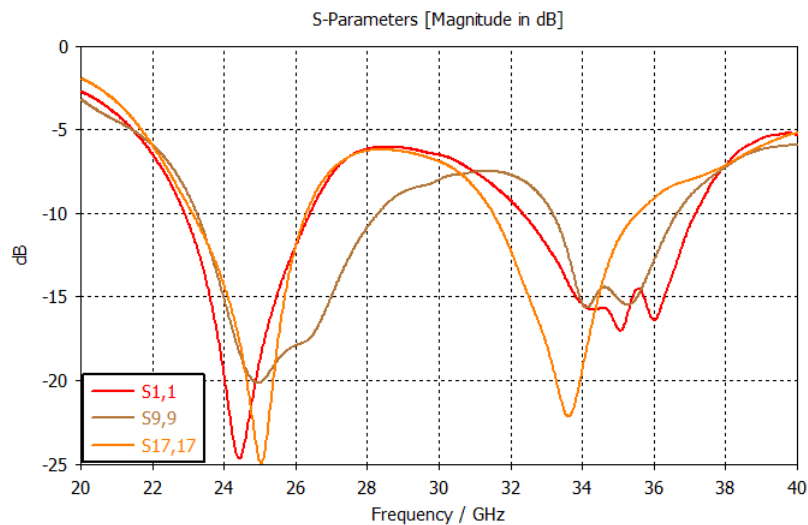
Figure 5.30: S parameters (3x3 array without profile, dual coax fed)

The better matching of the edge elements upon using the profile is due to the fact that the profile reduces the edge diffraction by more effectively confining the EM waves within the DRA thus leading to better matching. To improve the performance of the edge elements (for array with homogeneous permittivity), we add a layer of dummy elements around the array. These are elements that are exactly the same as that in the array, but are not excited during operation. This means the effective array size becomes 5x5. The improvement in the performance can be seen in the figure below, where all the elements are matched better (performance similar to that at single element level). Two layers of dummy elements was also investigated but the performance remained the same hence the number of dummy element layers was kept at 1.

This leads us to the conclusion that making use of permittivity profiles can enable improved performance in a smaller array footprint.
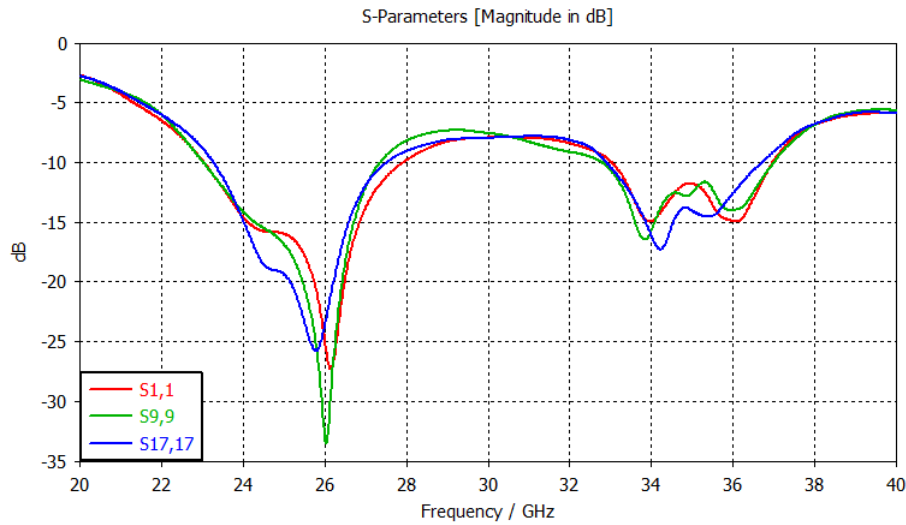
Figure 5.31: S parameters (3x3 array without profile, with dummy elements)

Now the mutual coupling between the ports within the same element, for the centre and edge elements are observed. As observed at the element level, the incorporation of a profile enables mitigation of the coupling which can be viewed in the plots below. The coupling in the latter model reaches as high as -5 dB across the operational band. However, the coupling between the elements are not seen to vary significantly and is consistently below -12 dB for both the cases.
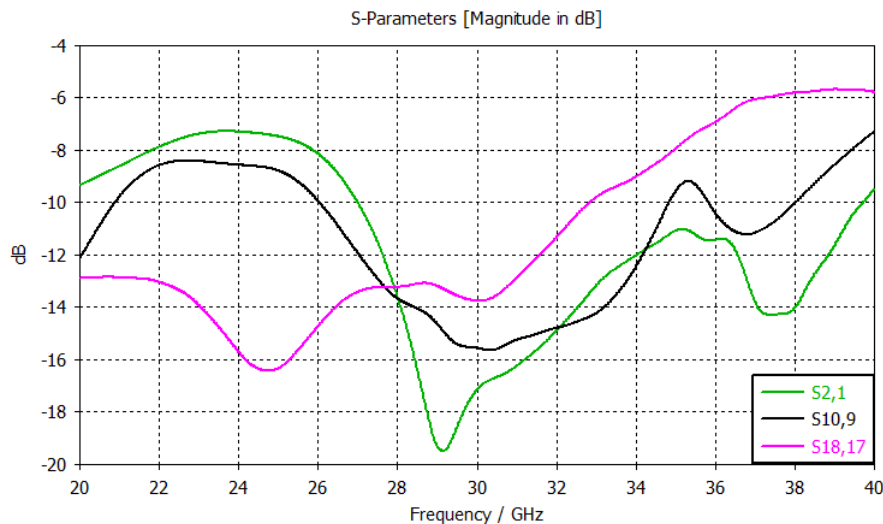
Figure 5.32: Coupling (within element), 3x3 array with profile
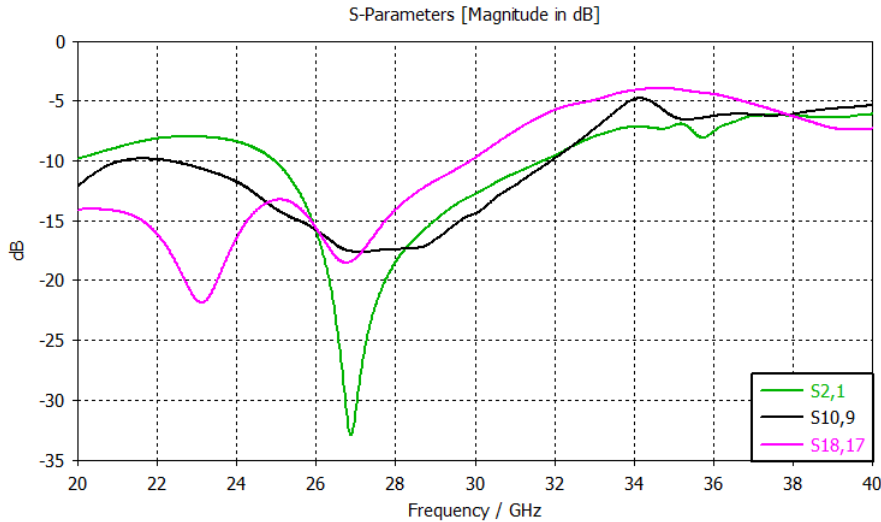
Figure 5.33: Coupling (within element), 3x3 array without profile

5.5. Comparison of feeding techniques

Here we make a comparison of the two feeding techniques investigated here, namely probe fed and aperture coupling. Although it faces fabrication constraints, the probe feeding was used for the purpose of studying the benefits of permittivity profiles. This type of feeding is utilized to study the coupling between the probes and also as circular polarization can be generated relatively easily by using a dual probe configuration.

In order to demonstrate the feasibility of employing tailored permittivity at mm-wave frequencies, models were developed with the intention of subsequent fabrication. The utilization of slot feeding enables efficient coupling of electromagnetic energy into the DRA while maintaining the desired linear polarization. Moreover, this feeding method facilitates the fabrication process and contributes to the overall ease of manufacturing the DRA, while providing better polarization purity and higher gain. These can further be seen in the table below

Feeding type	Impedance bandwidth (%)	Realized Gain (dBi)	Cross- polarization (θ=0) (dBi)
Probe feeding	46.36	6.6	-8.13
Slot feeding	30.1	7.9	-75

Table 5.8: Probe vs slot feeding (single linear polarization)

For CP operations, dual probe configuration is preferred as it helps obtain a wider axial ratio bandwidth, as opposed to a cross slot technique. Such a cross slot technique was investigated by [45] to excite a CDRA and it was observed that the axial ratio bandwidth was very narrow at 3.91%. Hence to keep the focus on permittivity profiles and to draw comparisons, fabrication constraints were overlooked and dual probe feeding was employed for the simulations. The disparity between the bandwidth of both the cases could be due to a sub optimal design of the slot fed model.

5.6. Comparison of single element prototypes (homogeneous permittivity vs profile)

At a single element level, two slot-fed models were designed for fabrication,n one with a vertically ascending permittivity profile (ϵ_{min} = 3, ϵ_{max} = 7) and another one with a homogeneous permittivity of 5.5. The DRAs are operated in single linear polarization and the impedance bandwidth and gain are examined. It is observed that the impedance bandwidths for the models with and without a profile are at 30.12% and 21.1% respectively (Figure 5.34). Therefore introducing a profile is beneficial as it improves the fractional bandwidth by 9%. The realized gain however is found to be almost the same for both cases with the latter design having a slightly higher ($\sim$ 0.4 dB more) overall peak gain at 8.3 dB. The cross-polarization is also examined to be the same at broadside. Upon plotting the realized gain across the frequency range, we see that gain is stable over a wider range of frequency upon employing a permittivity profile (Figure 5.35).
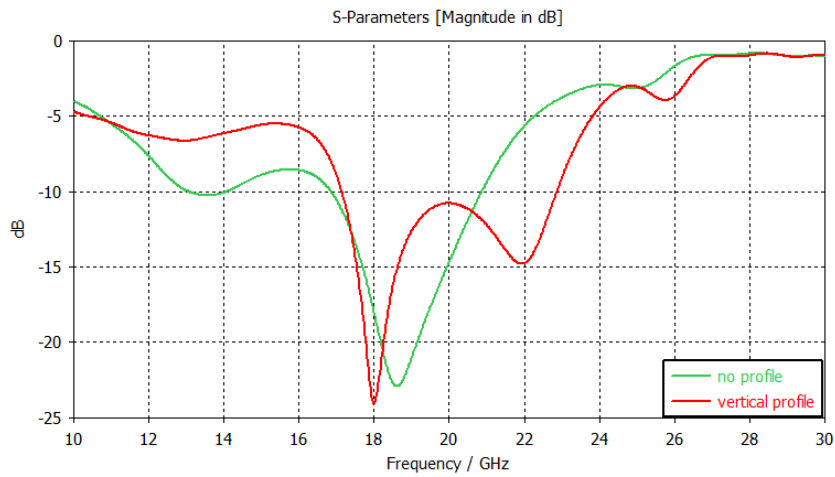
Figure 5.34: S1,1 comparison (profile 1 vs homogeneous permittivity, single element, slot fed)

Figure 5.35: Gain vs Frequency comparison (profile 1 vs homogeneous permittivity, single element, slot fed)

5.7. Comparison of 1x9 array prototypes (homogeneous permittivity vs profile)

The designs with profile 1 and uniform permittivity, both in a linear array environment of 9 elements are compared in this section. Here primarily the scan performance is compared. We look into the matching of the active S-parameters upon scanning from $0°$ to $45°$.

Firstly, the gain vs frequency at broadside is observed at both the cases (Figure 5.36). The array with the profile incorporated has a reduced overall peak gain, however the gain is more stable over a wider frequency range.
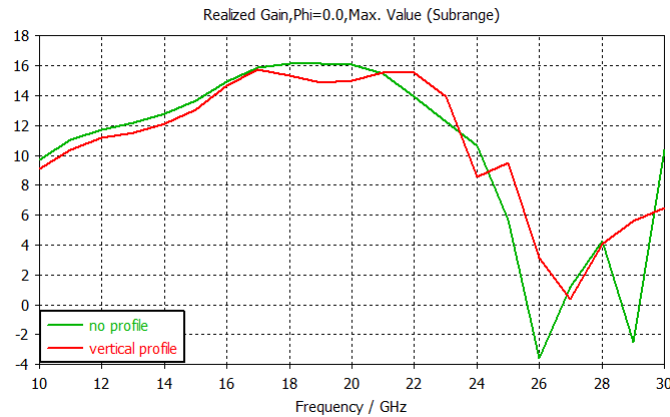
Figure 5.36: Gain vs Frequency comparison

To observe the matching of the elements upon scanning, the active S parameters curves for a centre element, edge element and a middle element are plotted. The port definitions are seen in Figure 4.14.

(a) Vertical Profile   **(b)** No profile
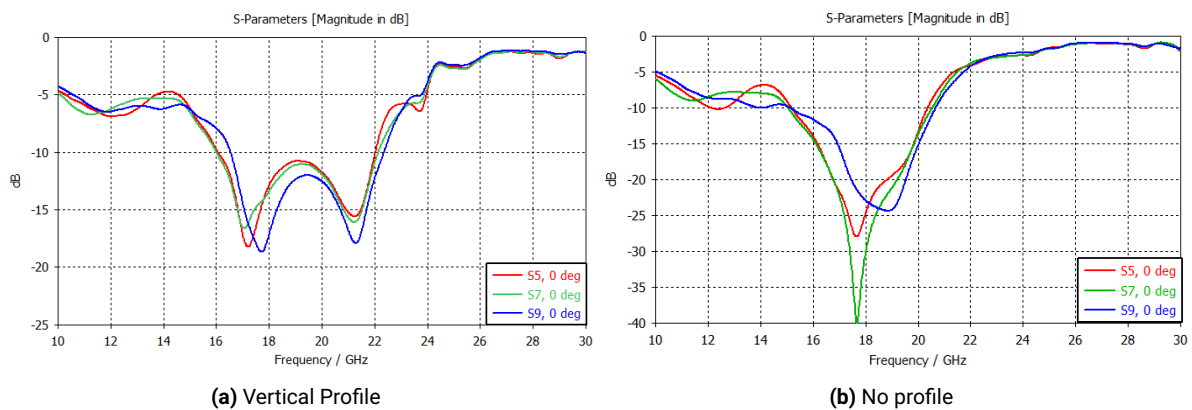
Figure 5.37: Active S parameters ($0°$)

We see that upon scanning, the array which does not use the profile loses the matching over the frequency band. This can be attributed to the coupling (over the air) between the elements. In contrast, the matching of the elements are maintained when the profile is used. The better matching seen at larger scan angles is a result of the profile enabling better confinement of fields inside the DRA, thereby mitigating the effect of coupling between the elements

(a) Vertical Profile

(b) No profile
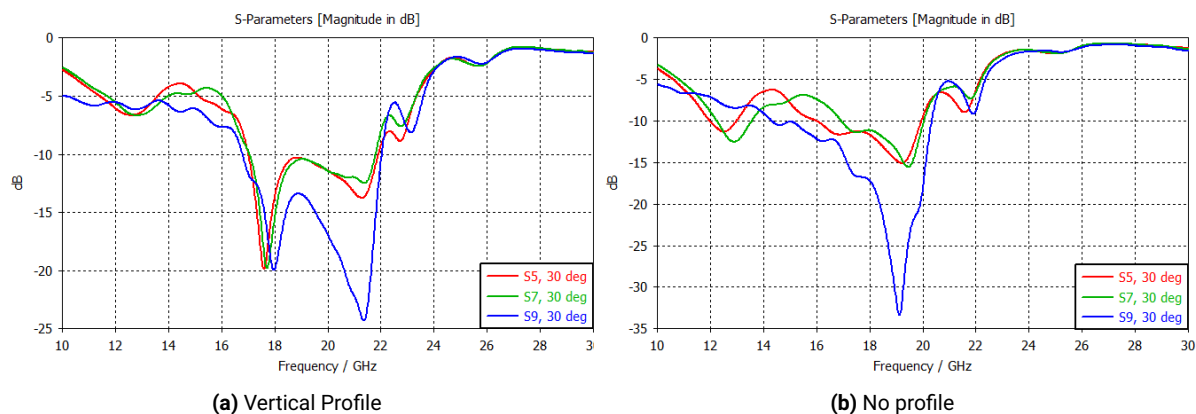
Figure 5.38: Active S parameters (30°)

(a) Vertical Profile

(b) No profile
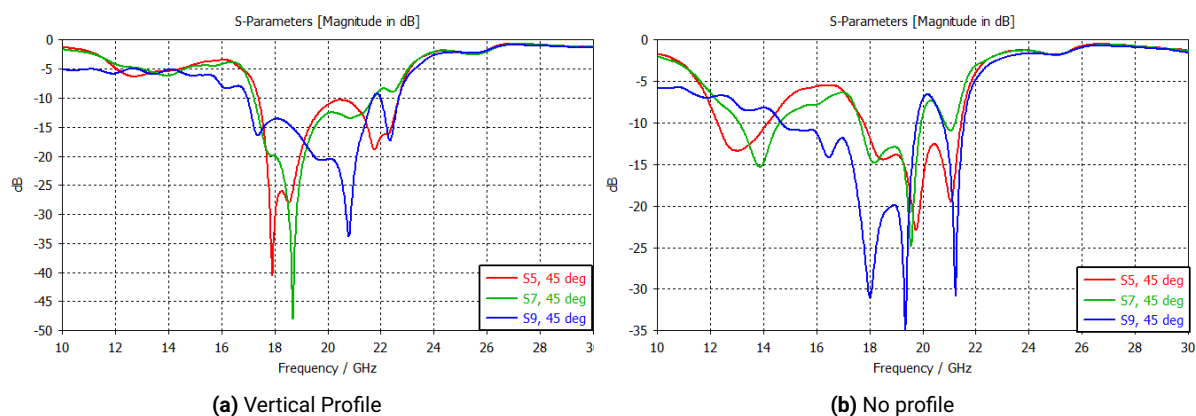
Figure 5.39: Active S parameters (45°)

that could cause mismatches at larger scan angles.

The gain vs scan angle at 22 and 23 GHz (edge of the band) is plotted for both the cases. It is observed that at 23 GHz, the drop in gain from 0 to 45 degrees is more gradual for the profiled array, whereas the drop is sharper when a homogeneous permittivity is employed. Nevertheless it is observed that for both frequencies, the profiled model exhibits a higher overall gain during scanning.

(a) Gain vs Scan angle (22 GHz)

(b) Gain vs Scan angle (23 GHz)
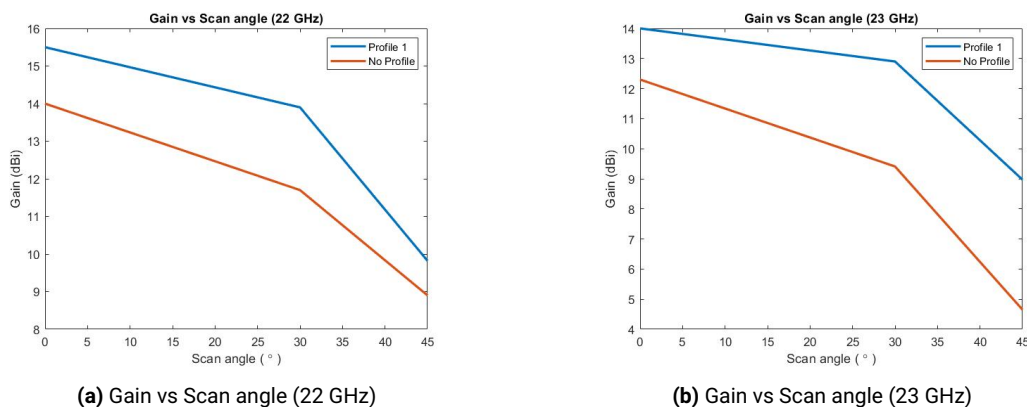
Figure 5.40: Gain vs Scan angle plots

6

Fabrication and Measurements

The fabrication of the prototypes is done using the fabrication facilities at the **German Aerospace Center (DLR)**, Wessling Germany. The images of the fabricated prototypes and feed networks, both at single element and 1x9 array level are shown below.
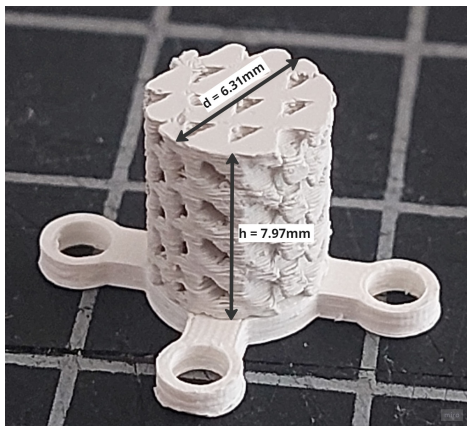
(a) Fabricated CDRA with permittivity profile (single element)
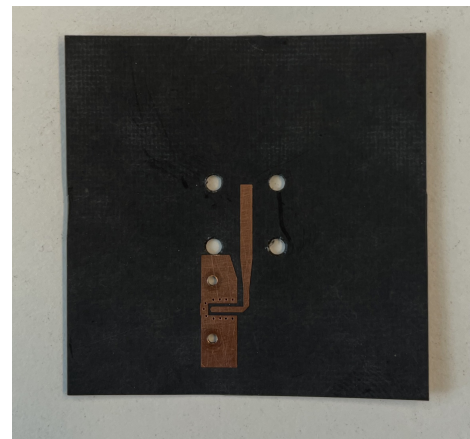
(b) Printed feed network (single element)

Figure 6.1: Single element DRA and feed network
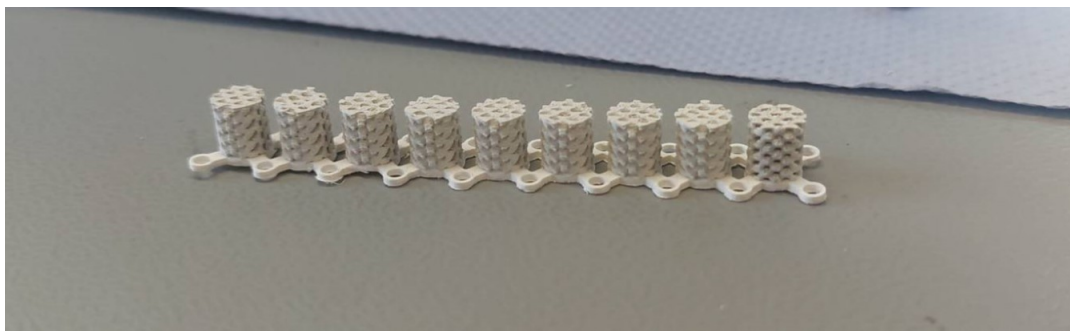
Figure 6.2: Fabricated CDRA array with permittivity profile (1x9)
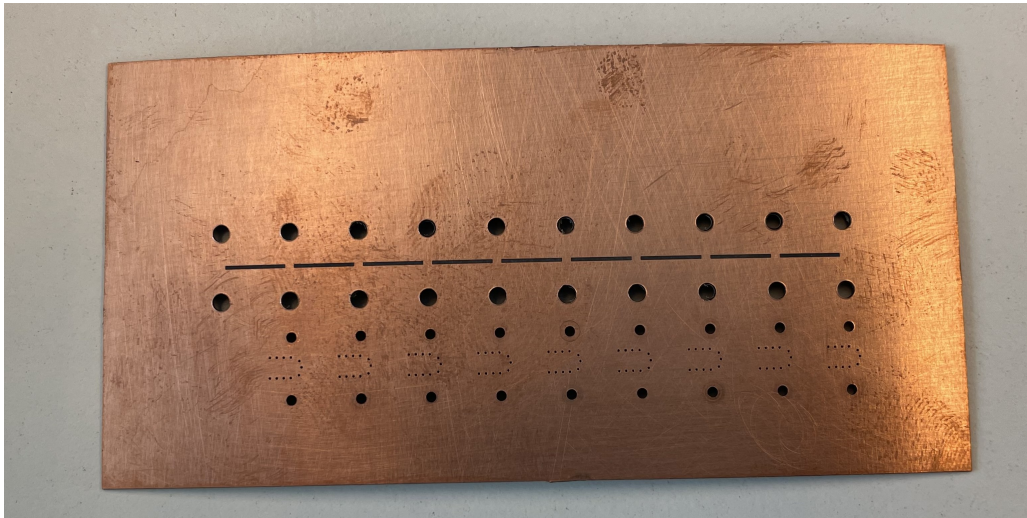
Figure 6.3: Feed network for array (top)

Figure 6.4: Feed network for array (bottom)

Due to lack of time to conduct measurements, the results from the same will further be presented and analyzed in an IEEE conference publication.

7

Conclusion and Recommendations

This chapter summarizes the key results and contributions to existing literature. The areas for future research are also listed in this part.

7.1. Conclusion

This thesis presents a novel design idea for DRAs at mm-wave frequencies (25 - 35 GHz) with a swept permittivity. A comparative analysis of various permittivity profiles in mm-wave DRAs achievable by means of additive manufacturing techniques is also done for the first time in this thesis. The benefits of using permittivity profiles are highlighted by making a fair comparison with a benchmark design with a homogeneous permittivity. Moreover, the impact of such profiles in an array environment is studied for the first time in this work.

Firstly, a novel comparison of different permittivity profiles at the single-element level is carried out. In total, six profiles were designed. The selection of these profiles aimed to explore and analyze the effects of both linear and non-linear permittivity profiles. The objective was to examine the corresponding field distribution and resulting performances when the maximum permittivity occurs at various points within the DR (Dielectric Resonator) geometry. The vertically ascending profile (1) and the non-linear profile (5) were found to be compelling candidates. Although both these profiles performed very similar in CP operation, Profile 1 had an edge over the latter in terms of impedance bandwidth in LP operation ($\sim 2\%$ improvement). In the case of Profile 1, a smoother transition in the wave impedance within the DR resulted in better matching and thus improved impedance bandwidth. As the final prototype was also designed for LP operation, Profile 1 was chosen for all further comparative analyses.

Secondly, a first time fair comparison (same DRA dimensions) of a design having a permittivity profile (1) with a benchmark homogeneous permittivity model is made. For this purpose, a benchmark model with a permittivity of 6.5 was designed. Here, the permittivity is chosen such that a performance in a similar frequency band (30 GHz) is obtained while keeping all the

dimension parameters constant to ensure a fair comparison. It was observed that the design with the profile outperformed the benchmark model across all performance metrics. In case of the design without a profile, the fields within the DR are distributed more uniformly throughout whereas the profile allows for the tailoring of the field distribution resulting in lower coupling. The improvement in the bandwidth, gain and axial ratio are results of this mitigated coupling between the ports. The following Table 7.1 summarizes the comparison of both the models at a single element level:

Performance metric	Model	
	Profile 1 (vertically ascending)	Benchmark model (ϵ_r = 6.5)
Impedance bandwidth (single port excitation) (%)	46.36	39.2
Impedance bandwidth (dual port excitation) (%)	45.28	33.06
Co-polarization (θ = 0) (dBi)	6.52	5.65
Cross polarization (θ = 0) (dBi)	-8.14	-5.84
Axial Ratio Bandwidth (%)	25	15.5

Table 7.1: Comparison with benchmark model

Finally, the study of profiled DRAs in an array setting is done for the first time. The models are extended to a 3x3 array to observe the array performance. It was noted that the performance of the edge elements deteriorated when employing elements with homogeneous permittivity. On the contrary, the use of tailored permittivity did not affect the make the matching of the edge elements by reducing spurious radiation at the edges and hence there was no degradation in the performance. The better matching of the edge elements on using the permittivity profile can be attributed to the better confinement of EM waves within the DRA thus reducing unnecessary edge diffraction.

For fabrication purposes, slot fed models intended for a single linearly polarized operation are prepared (operational band: 17-21 GHz, due to fabrication limitations). These elements are then extended to a linear array of 1x9 elements, where the scan performance is observed. It is seen that upon scanning from $0°$ to $45°$, the active S parameters of the elements are better matched (within the whole operational band) when the profile is used. This is also a result of the better field confinement achieved by using a profile, resulting in mitigated coupling (over the air) between the elements upon scanning.

The outcomes obtained from the prototype measurements (single element and 1x9 array) will be subsequently presented and analyzed in a forthcoming IEEE conference publication.

7.2. Recommendations

The following areas can be considered as recommendations for an extension to this work:

- Further exploration on different profile designs and their impact on the performance of array systems. Moreover, the profiles discussed here can be incorporated into more complex shaped DRAs like supershapes.

- Further optimization of array configurations, such as element spacing and arrangement can be done to improve array performance and efficiencies.

- Investigating innovative manufacturing techniques and novel materials for profile-based array systems can help to improve fabrication processes and performance.

- Research on calibration methods and beamforming algorithms specifically adapted for profile-based array systems to enhance performance and achieve precise radiation control.

- Employing Frequency Selective Surfaces (FSS) to improve the scan performance of such profile-based arrays.

A
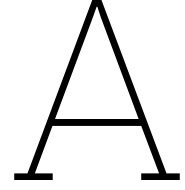
Modes in a CDRA

For a CDRA of radius a and height h, the field distributions can be expressed in terms of Bessel functions as:

$$TE: \quad H_z^{npm} = Jn \left\langle \left(X_{np}^{TE} r\right) \mid a \right\rangle \left\{ \begin{array}{c} \sin(n\phi) \\ \cos(n\phi) \end{array} \right\} \sin[(2m+1)\pi z/2h]\}$$

$$TM: \quad E_z^{npm} = Jn \left\langle \left(X_{np}^{TM} r\right) \mid a \right\rangle \left\{ \begin{array}{c} \sin(n\phi) \\ \cos(n\phi) \end{array} \right\} \cos[(2m+1)\pi z/2h]\} \tag{A.1}$$

$$n = 1, 2, 3 \dots \quad p = 1, 2, 3 \dots \dots \quad m = 0, 1, 2 \dots \dots$$

where J_n is the nth order of the Bessel function of the first kind while (X_{np}^{TE}) and (X_{np}^{TM}) are roots that satisfy the equations: $J_n(X_{np}^{TE})$ = 0 and $J_n(X_{np}^{TM})$ = 0
A more simplified expression for the resonant mode frequency is given by the equation

$$f_{npm} = \frac{C}{2\pi a \sqrt{\varepsilon_r}} \sqrt{\left\{ \begin{array}{c} X_{np}^{TE^2} \\ X_{np}^{TM^2} \end{array} \right\} + \left[\frac{\pi a}{2d}(2m+1)\right]^2} \tag{A.2}$$

The estimations of the field components of the $HEM_{11\delta}$ mode of the CDRA is given as [46, 47, 48]:

$$E_Z \propto J_1(\alpha r) \cos\left(\frac{\pi z}{2h}\right) \left\{ \begin{array}{c} \cos\phi \\ \sin\phi \end{array} \right\}$$

$$E_r \propto \frac{\partial J_1(\alpha r)}{\partial(\alpha r)} \sin\left(\frac{\pi z}{2h}\right) \left\{ \begin{array}{c} \cos\phi \\ \sin\phi \end{array} \right\} \tag{A.3}$$

$$E_\phi \propto J_1(\alpha r) \sin\left(\frac{\pi z}{2h}\right) \left\{ \begin{array}{c} \sin\phi \\ \cos\phi \end{array} \right\}$$

$$H_r \propto J_1(\alpha r) \cos\left(\frac{\pi z}{2h}\right) \left\{ \begin{array}{c} \sin\phi \\ \cos\phi \end{array} \right\}$$

$$H_\phi \propto \frac{\partial J_1(\alpha r)}{\partial(\alpha r)} \cos\left(\frac{\pi z}{2h}\right) \left\{ \begin{array}{c} \cos\phi \\ \sin\phi \end{array} \right\} \qquad \text{(A.4)}$$

$$H_z \approx 0$$

where J_1 is the 1st order Bessel function of the first kind, α is the solution to $J_1(\alpha a) = 0$ and a is the radius of the CDRA. The choice of $\sin\phi$ and $\cos\phi$ are determined by the location of the feed.

The TE mode can be supported only if the DRA is placed on a magnetic conductor ground plane. However, this is not physically possible [49, 50]. For the TE mode to be excited, the CDRA axis and the current direction should be perpendicular to each other. Hence they can only be excited in a configuration where the CDRA axis is parallel to the ground plane, as shown in figure A.1
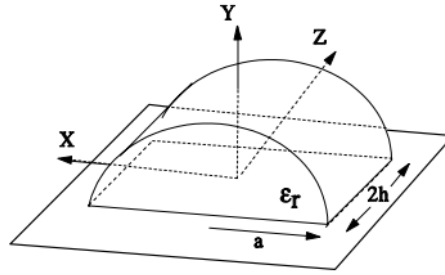
Figure A.1: Half-Split Cylindrical DRA geometry [49]

The field estimations of the $TE_{01\delta}$ mode are given by [51, 52, 53] as follows:

$$H_z \propto J_0(\beta r) \cos\left(\frac{\pi z}{2h}\right)$$
$$H_r \propto J_1(\beta r) \sin\left(\frac{\pi z}{2h}\right)$$
$$E_\phi \propto J_1(\beta r) \cos\left(\frac{\pi z}{2h}\right) \qquad \text{(A.5)}$$
$$E_Z = E_r = H_\phi = 0$$

Here, J_0 and J_1 are the zeroth and first order Bessel functions of the first kind respectively. β is obtained as a solution to $J_1(\beta a) = 0$ with a as the radius.

The $TM_{01\delta}$ mode has similar fields except that the E and H fields are interchanged.

Bibliography

[1] S. A. Long, M. W. McAllister, and L. C. Shen, "The resonant cylindrical dielectric cavity antenna," *IEEE Transactions on Antennas and Propagation*, vol. 31, pp. 406–412, May 1983.

[2] D. Guha and C. Kumar, "Microstrip patch versus dielectric resonator antenna bearing all commonly used feeds: An experimental study to choose the right element," *IEEE Antennas and Propagation Magazine*, vol. 58, pp. 45–55, 2 2016.

[3] N. K. Mishra, S. Das, and D. K. Vishwakarma, "Beam steered linear array of cylindrical dielectric resonator antenna," *AEU - International Journal of Electronics and Communications*, vol. 98, pp. 106–113, 2019.

[4] D. Caratelli, A. Al-Rawi, J. Song, and D. Favreau, "Dielectric resonator antenna arrays for 5g wireless communications," *Microwave Journal*, 2020.

[5] S. Keyrouz and D. Caratelli, "Dielectric resonator antennas: Basic concepts, design guidelines, and recent developments at millimeter-wave frequencies," *International Journal of Antennas and Propagation*, vol. 2016, 2016.

[6] F. Wang, C. Zhang, H. Sun, and Y. Xiao, "Ultra-wideband dielectric resonator antenna design based on multilayer form," *International Journal of Antennas and Propagation*, vol. 2019, 2019.

[7] Z. X. Xia, K. W. Leung, and K. Lu, "3-d-printed wideband multi-ring dielectric resonator antenna," *IEEE Antennas and Wireless Propagation Letters*, vol. 18, pp. 2110–2114, 10 2019.

[8] J.-I. Moon and S.-O. Park, "Dielectric resonator antenna for dual-band pcs/imt-2000," *Electronics Letters*, vol. 36, no. 12, pp. 1002–1003, 2000.

[9] M. Simeoni, R. Cicchetti, A. Yarovoy, and D. Caratelli, "Plastic-based supershaped dielectric resonator antennas for wide-band applications," *IEEE Transactions on Antennas and Propagation*, vol. 59, pp. 4820–4825, 12 2011.

[10] A. Kesavan, M. Al-Hassan, I. B. Mabrouk, and T. A. Denidni, "Wideband circular polarized dielectric resonator antenna array for millimeter-wave applications," *Sensors*, vol. 21, 6 2021.

[11] H. Xu, Z. Chen, H. Liu, L. Chang, T. Huang, S. Ye, L. Zhang, and C. Du, "Single-fed dual-circularly polarized stacked dielectric resonator antenna for k/ka-band uav satellite communications," *IEEE Transactions on Vehicular Technology*, vol. 71, pp. 4449–4453, 4 2022.

[12] Z. L. Su, K. W. Leung, and K. Lu, "A shaped-beam antenna for wide-angle scanning phased array," *IEEE Transactions on Antennas and Propagation*, vol. 70, pp. 7659–7669, 9 2022.

[13] G. Massie, M. Caillet, M. Clénet, and Y. M. Antar, "A new wideband circularly polarized hybrid dielectric resonator antenna," *IEEE Antennas and Wireless Propagation Letters*, vol. 9, pp. 347–350, 2010.

[14] N. Ojaroudiparchin, M. Shen, and G. F. Pedersen, "Mm-wave dielectric resonator antenna (dra) with wide bandwidth for the future wireless networks," Institute of Electrical and Electronics Engineers Inc., 6 2016.

[15] J. Moon and S. Park, "Dielectric resonator antenna for dual-band pcs/imt-2000," *Electronics Letters*, vol. 36, pp. 1002–1003, 2000.

[16] L. Y. Feng, D. B. Msilanga, A. M. Sadiq, and S. Wang, "Dielectric resonator antenna for wide millimeter-wave band; dielectric resonator antenna for wide millimeter-wave band," 2018.

[17] B. Liu, J. Qiu, N. Wang, and G. Li, *Circularly Polarized Pyramid Dielectric Resonator Antenna with Single Aperture Fed*.

[18] M. Simeoni, R. Cicchetti, A. Yarovoy, and D. Caratelli, "Supershaped dielectric resonator antennas," in *2009 IEEE Antennas and Propagation Society International Symposium*, pp. 1–4, 2009.

[19] J. Gielis, "A generic geometric transformation that unifies a wide range of natural and abstract shapes," *American journal of botany*, vol. 90, pp. 333–8, 03 2003.

[20] M. Tang and J.-F. M. H.-D. Wen, *A Wideband Circularly Polarized Anisotropic Dielectric Resonator Antenna with Improved Gain*.

[21] S. Deng and C.-L. Tsai, "A broadband slot-coupled circularly polarized rectangular notch dielectric resonator antenna fed by a microstrip line," *2005 IEEE Antennas and Propagation Society International Symposium*, vol. 4B, pp. 246–249 vol. 4B, 2005.

[22] K. X. Wang and H. Wong, "A circularly polarized antenna by using rotated-stair dielectric resonator," *IEEE Antennas and Wireless Propagation Letters*, vol. 14, pp. 787–790, 2015.

[23] Y. Liu, Y. Jiao, Z. Weng, C. Zhang, and H. Zhang, "A high-gain dielectric resonator antenna array fed by back-cavity," pp. 1–3, Institute of Electrical and Electronics Engineers Inc., 6 2018.

[24] M. T. Hussain, O. Hammi, M. S. Sharawi, S. K. Podilchak, and Y. M. Antar, "A dielectric resonator based millimeter-wave mimo antenna array for hand-held devices," vol. 2015-October, pp. 3–4, Institute of Electrical and Electronics Engineers Inc., 10 2015.

[25] Y. Mandkea and R. Henryb, "Review of additive manufacturing 3d printed microwave components for rapid prototyping," 2017.

[26] D. Helena, A. Ramos, T. Varum, and J. N. Matos, "Antenna design using modern additive manufacturing technology: A review," *IEEE Access*, vol. 8, pp. 177064–177083, 2020.

[27] J. Kowalewski, A. Jauch, J. Eisenbeis, S. Marahrens, K. Schneider, and T. Zwick, "Dual-polarized dielectric resonator antenna array for 5g mobile radio base stations; dual-polarized dielectric resonator antenna array for 5g mobile radio base stations," 2020.

[28] F. P. Chietera, R. Colella, and L. Catarinucci, "Dielectric resonators antennas potential unleashed by 3d printing technology: A practical application in the iot framework," *Electronics (Switzerland)*, vol. 11, 1 2022.

[29] G. Brennecka and P. Nayeri, *Wideband 3D-Printed Dielectric Resonator Antennas*. 2018.

[30] C. Yang, Y. Xiao, and K. W. Leung, "A 3d-printed wideband multilayered cylindrical dielectric resonator antenna with air layers," vol. 2020-December, pp. 561–563, Institute of Electrical and Electronics Engineers Inc., 12 2020.

[31] C. Balanis, *Antenna Theory: Analysis and Design*. Wiley, 2016.

[32] C. A. Balanis, *Advanced Engineering Electromagnetics, 2nd Edition*. John Wiley & Sons, 2012.

[33] J. Volakis, *Antenna Engineering Handbook, Fourth Edition*. McGraw-Hill Professional, 2007.

[34] Y. Kobayashi and S. Tanaka, "Resonant modes of a dielectric rod resonator short-circuited at both ends by parallel conducting plates," *IEEE Transactions on Microwave Theory and Techniques*, vol. 28, no. 10, pp. 1077–1085, 1980.

[35] A. Petosa, *Dielectric Resonator Antenna Handbook*. Artech House antennas and propagation library, Artech House, 2007.

[36] Y. He, C. Gu, H. Ma, J. Zhu, and G. Eleftheriades, "Miniaturized circularly polarized doppler radar for human vital sign detection," *IEEE Transactions on Antennas and Propagation*, vol. 67, pp. 7022–7030, 2019.

[37] G. Almpanis, C. Fumeaux, and R. Vahldieck, "Offset cross-slot-coupled dielectric resonator antenna for circular polarization," *IEEE Microwave and Wireless Components Letters*, vol. 16, no. 8, pp. 461–463, 2006.

[38] A. Laisne, R. Gillard, and G. Piton, "Circulary polarised dieletric resonator antenna with metallic strip," *Electronics Letters*, vol. 38, pp. 106 – 107, 03 2002.

[39] K. Leung, W. Wong, and H. Ng, "Circularly polarized slot-coupled dielectric resonator antenna with a parasitic patch," *IEEE Antennas and Wireless Propagation Letters*, vol. 1, pp. 57–59, 2002.

[40] L. Baggen, S. Holzwarth, W. Simon, and O. Litschke, "Phased array using the sequential rotation principle: Analysis of coupling effects," pp. 571 – 576, 11 2003.

[41] Y. Mandke and R. Henry, "Review of additive manufacturing 3d printed microwave components for rapid prototyping," 03 2017.

[42] S. Wickramasinghe, T. Do, and P. Tran, "Fdm-based 3d printing of polymer and associated composite: A review on mechanical properties, defects and treatments," *Polymers*, vol. 12, no. 7, 2020.

[43] J. Huang, Q. Qin, and J. Wang, "A review of stereolithography: Processes and systems," *Processes*, vol. 8, no. 9, 2020.

[44] S. P. Hehenberger, S. Caizzone, and A. G. Yarovoy, "Additive manufacturing of linear continuous permittivity profiles and their application to cylindrical dielectric resonator antennas," *IEEE Open Journal of Antennas and Propagation*, vol. 4, pp. 373–382, 2023.

[45] C.-Y. Huang, J.-Y. Wu, and K.-L. Wong, "Cross-slot-coupled microstrip antenna and dielectric resonator antenna for circular polarization," *IEEE Transactions on Antennas and Propagation*, vol. 47, no. 4, pp. 605–609, 1999.

[46] M. W. McAllister, S. A. Long, and G. L. Conway, "Rectangular dielectric resonator antenna," *Electron. Lett.*, vol. 19, p. 218, March 17 1983.

[47] M. Zou and J. Pan, "Investigation of resonant modes in wideband hybrid omnidirectional rectangular dielectric resonator antenna," *IEEE Transactions on Antennas and Propagation*, vol. 63, pp. 1–1, 07 2015.

[48] J. Gupta, B. Mukherjee, and N. Gupta, "A novel tetraskelion dielectric resonator antenna for wideband applications," *Microwave and Optical Technology Letters*, vol. 57, no. 12, pp. 2781–2786, 2015.

[49] K. Luk and M. K. W. Leung, *Dielectric Resonator Antennas*. England: Research Studies Press Ltd., 2003.

[50] A. Petosa and A. Ittipiboon, "Dielectric resonator antennas: A historical review and the current state of the art," *IEEE Antenna and Propagation Magazine*, vol. 52, no. 5, pp. 91–116, 2010.

[51] J. C. Sethares and J. Nauman, "Design of microwave dielectric resonators," *IEEE Transactions on Microwave Theory and Techniques*, vol. 14, no. 1, pp. 2–7, 1966.

[52] D. Kafez and P. Guillon, eds., *Dielectric Resonators*. Norwood, MA: Artech House, 1986.

[53] N. Gupta, S. K. Rout, and K. Sivaji, "Characteristics of cylindrical dielectric resonator antenna," *Microwave Review*, vol. 15, no. 2, pp. 29–32, 2009.